Computational Mechanics (2024) 73:795–829
https://doi.org/10.1007/s00466-023-02390-z

ORIGINAL PAPER

Homogenization assumptions for the two-scale analysis of first-order shear deformable shells

Leonie Mester[1] · **Simon Klarmann**[1] · **Sven Klinkel**[1]

Received: 21 December 2022 / Accepted: 28 August 2023 / Published online: 22 September 2023

Abstract
This contribution presents a multiscale approach for the analysis of shell structures using Reissner–Mindlin kinematics. A distinctive feature is that the thickness of the representative volume element (RVE) corresponds to the shell thickness. The main focus of this paper is on the choice of correct boundary conditions for the RVE. Three different types of boundary conditions, which fulfil the Hill–Mandel condition, are presented to bridge the two scales. A common feature is the application of zero-traction boundary conditions at the top and bottom surfaces of the RVE. Furthermore, an internal constraint is used to reduce the dependency of the stiffness components on the RVE size. The introduced boundary conditions differ mainly in the application of shear strains and their symmetry requirements on the RVE. The characteristic features are compared by means of linear-elastic benchmark tests. It is shown that the stress resultants and tangent stiffness components are obtained correctly. Moreover, the presented approach is verified using different macroscopic shell structures and different mesostructures. Both, linear and nonlinear small strain examples are compared to analytical values or full-scale solutions and demonstrate a wide applicability of the present formulation.

Keywords Homogenization · RVE boundary conditions · Reissner–Mindlin shell · FE^2

1 Introduction

Novel, highly engineered composite materials allow the optimal utilisation of specific material properties. For example, textile-reinforced composite materials can be used for the design of slender structures, motivating the use of shell formulations for analysis. The periodicity of the textile reinforcement allows for the choice of a representative volume element (RVE) to describe the meso-structural behaviour. Because full-scale models, which approximate the entire structure, are often computationally expensive, the use of a multiscale method, which determines the effective material properties, is justified.

✉ Leonie Mester
mester@lbb.rwth-aachen.de

Simon Klarmann
klarmann@lbb.rwth-aachen.de

Sven Klinkel
klinkel@lbb.rwth-aachen.de

[1] Chair of Structural Analysis and Dynamics, RWTH Aachen University, Mies-van-der-Rohe-Str. 1, Aachen 52074, Germany

Many different computational homogenization methods have been developed, extensive overviews can be found, for example, in [18, 35]. One of them is the FE^2 method, which has been first introduced by Feyel and Chaboche [16]. To each macroscopic integration point, a separate representative volume element is related, on which a boundary value problem has to be solved. The method is computationally expensive but can be parallelized for the microscale, see e.g. [21], and further enhanced by an adaptive approach [34]. Generally, there are two different approaches to computational homogenization. The first introduced scheme was the first-order computational homogenization where only the deformation gradient is used for scale transition. This has been extended by additionally using the strain gradient in the framework of second-order homogenization. The latter aims to capture size effects on the mesoscopic scale and higher-order deformation modes. The two scales are classically coupled by the Hill–Mandel condition, which ensures the equality of virtual work on both scales [24]. Based on this requirement, different boundary conditions can be defined. As an alternative to the Hill–Mandel homogenization, which is widely used, a homogenization scheme for structural elements based on the Irving-Kirkwood theory has been proposed recently [31].

The combination of computational homogenization with structural components on the macroscopic scale is a wide field of research, see [4, 28] for beam kinematics and [11, 17, 21–23] for shell structures. While [21, 22] consider a first-order computational homogenization approach, [11, 17, 23] are concerned with second-order approaches. One of the main characteristics is, that the RVE extends through the whole thickness of the macroscopic structure. Therefore, the smaller scale will be referred to as mesoscale instead of microscale in the following. From the through-thickness extension of the RVE over the shell thickness an inconsistency arises when investigating shear deformable shells. The macroscopic shell models, e.g. Reissner–Mindlin kinematics, assume a zero through-thickness normal stress. However, this cannot be enforced using the classical RVE boundary conditions which can be derived from the Hill–Mandel condition. Furthermore, a dependency of the transverse shear stiffnesses on the RVE size is observed for example in [30]. Thus, a key point is the transfer of strains to the RVE.

While earlier publications validate the homogenization procedure only by means of complex examples and full-scale reference solutions [11, 12, 17], more recent publications focus on RVE benchmarks before investigating complex examples [22, 31, 38]. Different methods to overcome the observed inconsistency and length dependency of the homogenized stiffness components are proposed in the literature. Heller [22] focuses on the homogenization of sandwich composites with comb-like core structures and uses length-dependent shear correction factors to take the length dependency of the RVE into account. More recently Hii and El Said [23] examined a Reissner–Mindlin shell for a second-order homogenization framework. A volumetric constraint on the fluctuation moment was introduced to correctly apply the transverse shear strains. Alternatively, Börjesson et al [3] have introduced an anti-periodic fluctuation field in order to correct the twisting deformation. Allowing for the correct deformation modes reduces the length dependency of the torsional stiffness on the in-plane dimensions of the RVE.

The present work is based on the observations made by Klarmann et al [28] who has investigated the kinematic inconsistency for Timoshenko beams. A volumetric constraint is introduced which reduces the linear moment distribution across the RVE. In contrast to Hii and El Said [23] the constraint accounts for stiffness jumps over the cross-section. As consequence, the correct shear stiffnesses are obtained as homogenized values. Incorporation of the stiffness jumps does not affect the homogenization algorithm. The macroscopic shell strains are applied on the mesoscopic scale and the homogenized material tangent and stress resultants are returned. Since only standard inputs and outputs are used, any shell formulation can be used on the macroscopic scale.

Classically, the mesoscopic scale is analysed using the finite element method. In this contribution, scaled boundary isogeometric analysis (SBIGA) [8] is employed on the mesoscopic level so that the term 'FE-SBIGA' would be more precise than FE^2 for the present approach. However, the presented boundary conditions are also applicable for classical finite element discretisations. Isogeometric analysis was first introduced by Hughes et al [25] and has been applied to various engineering fields since. Its main advantage is the combination of modelling and analysis so that the geometrical approximation error can be overcome. This is particularly advantageous for complex mesostructures, such as textile reinforcement. In computer-aided design (CAD), solids are described by surfaces only. However, a three-dimensional tensor product is needed for the description of volumes [13]. One possibility to obtain these is the combination of IGA with the concepts of the scaled boundary finite element method (SBFEM) [36]. The boundaries from the surface description are scaled into one central point, denoted as scaling centre C. Following the fundamental SBFEM, the equilibrium is strongly applied in scaling direction. This leads to a second-order ordinary differential equation, which can be solved either analytically or numerically [9]. Alternatively, the weak form of equilibrium can be enforced in scaling direction, compare [10], to allow for the analysis of nonlinear problems. Here, the approach for 3D solids presented in [8] is employed. A bi-variate tensor product is used for the description of the boundary, while uni-variate B-Splines approximate the interior of the solid.

The present contribution proposes three different sets of boundary conditions for the lateral faces of the RVE in the scope of a first-order Hill–Mandel-based homogenization method, since the strain transfer between the scales is a key point in the computational homogenization of structural elements. Special attention is paid to the correct transfer of the transversal shear. The three boundary conditions impose different symmetry requirements on the RVE. Futheremore, they are compared each other and verified on the mesoscopic and macroscopic scale using analytical solutions or full-scale references solutions. Particular focus is given to heterogeneities which do not span the full width of the RVE, such as textile reinforcement. Internal constraints, based on the work of Klarmann et al [28], will be introduced for shell kinematics to overcome the observed kinematic inconsistency. Here, the mesostructure is analysed using SBIGA which allows the use of the exact geometry rather than an approximation. Furthermore, the three-dimensional nature of the mesostructure facilitates the employment of three-dimensional material laws.

The paper is organised as follows. Section 2 briefly discusses the macroscopic Reissner–Mindlin shell kinematics. On the mesoscopic scale, the scaled boundary isogeometric analysis is used which is recapitulated in Sect. 3. Section 4

presents the principles of Hill–Mandel-based homogenization and discusses the inconsistency concerning the transverse shear. The finite element formulations on both scales and the nested formulation involving both scales are given in Sect. 5. Section 6 introduces and compares three boundary conditions for the transfer of the macroscopic strains while Sect. 7 presents several numerical examples evaluating the mesoscopic scale and the overall multiscale approach.

2 Shell kinematics

The description of the shell kinematics follows the one in [21], where $\mathcal{B}_0$ is a shell with thickness h in the three-dimensional Euclidean space. The theory is limited to small strains, furthermore, inextensibility and zero normal stress in thickness direction are assumed. The initial reference surface (at $t = 0$) of the shell and its boundary are introduced as Ω_0 and Γ_0, respectively. Analogously, the current configuration of the shell $\mathcal{B}_t$ can be described by its reference surface Ω_t and its boundary Γ_t, compare Fig. 1. A convective coordinate system ξ^α, with $\alpha = 1, 2$, is introduced to describe the shell surface. Additionally, a thickness coordinate ζ ranging from $-\frac{h}{2} \leq \zeta \leq \frac{h}{2}$ is defined.

A director vector $\mathbf{D}$ is introduced as the unit normal vector to the reference surface Ω_0. By means of the rotational parameters $\boldsymbol{\omega}$, the director vector in the current configuration $\mathbf{d}$ is obtained. The inextensibility of the shell is enforced by $|\mathbf{D}| = |\mathbf{d}| = 1$. In the framework of Reissner–Mindlin shell theory, transversal shear strains are taken into account, for which $\mathbf{d} \neq \mathbf{n}$ applies. The rotational tensor $\mathbf{R}$ can be related to the rotational parameters $\boldsymbol{\omega}$ using the Euler-Rodrigues formula, thus $\mathbf{d} = \mathbf{R}\mathbf{D}$ holds.

Any point of the shell can be described by a position vector on the shell reference surface $\mathbf{X}(\xi^\alpha)$ and $\mathbf{x}(\xi^\alpha)$ for the initial and current configuration, respectively, and the director vectors. The relation in both configurations read

$$\begin{aligned} \boldsymbol{\Phi}(\xi^\alpha, \zeta) &= \mathbf{X}(\xi^\alpha) + \zeta\, \mathbf{D}(\xi^\alpha) \quad \text{and} \\ \boldsymbol{\phi}(\xi^\alpha, \zeta) &= \mathbf{x}(\xi^\alpha) + \zeta\, \mathbf{d}(\xi^\alpha). \end{aligned} \tag{1}$$

The displacement field $\mathbf{u}$ is derived as the difference of the position vectors in the shell space from Eq. 1 as

$$\mathbf{u} = \boldsymbol{\phi} - \boldsymbol{\Phi} = \underbrace{\mathbf{x} - \mathbf{X}}_{\mathbf{u}_0} + \zeta\ (\mathbf{d} - \mathbf{D})\,. \tag{2}$$

From the Green-Lagrange strain tensor $\mathbf{E} = E_{ij} = \frac{1}{2}\left(\boldsymbol{\phi}_{,i} \cdot \boldsymbol{\phi}_{,j} - \boldsymbol{\Phi}_{,i} \cdot \boldsymbol{\Phi}_{,j}\right)$ the shell strains

$$\boldsymbol{\varepsilon} = \left[\varepsilon_{11}\ \varepsilon_{22}\ 2\varepsilon_{12}\ \kappa_{11}\ \kappa_{22}\ 2\kappa_{12}\ \gamma_1\ \gamma_2\right]^{\mathrm{T}} \tag{3}$$

with the following components can be derived

$$\begin{aligned} \varepsilon_{\alpha\beta} &= \frac{1}{2}\left(\mathbf{x}_{,\alpha} \cdot \mathbf{x}_{,\beta} - \mathbf{X}_{,\alpha} \cdot \mathbf{X}_{,\beta}\right), \\ \kappa_{\alpha\beta} &= \frac{1}{2}(\mathbf{x}_{,\alpha} \cdot \mathbf{d}_{,\beta} + \mathbf{x}_{,\beta} \cdot \mathbf{d}_{,\alpha} - \mathbf{X}_{,\alpha} \cdot \mathbf{D}_{,\beta} - \mathbf{X}_{,\beta} \cdot \mathbf{D}_{,\alpha}), \\ \gamma_\alpha &= \mathbf{x}_{,\alpha} \cdot \mathbf{d} - \mathbf{X}_{,\alpha} \cdot \mathbf{D}\,. \end{aligned} \tag{4}$$

The second-order curvatures $\rho_{\alpha\beta}$ are neglected for thin shells. Here, Greek indices α, β range from 1 to 2 and Latin indices i, j, k range from 1 to 3. The Einstein summation convention is employed. Due to the inextensible director field, no normal strains in thickness direction occur. The shell strains can be related to the Green-Lagrange strains using the matrix $\mathbf{A}(\zeta)$

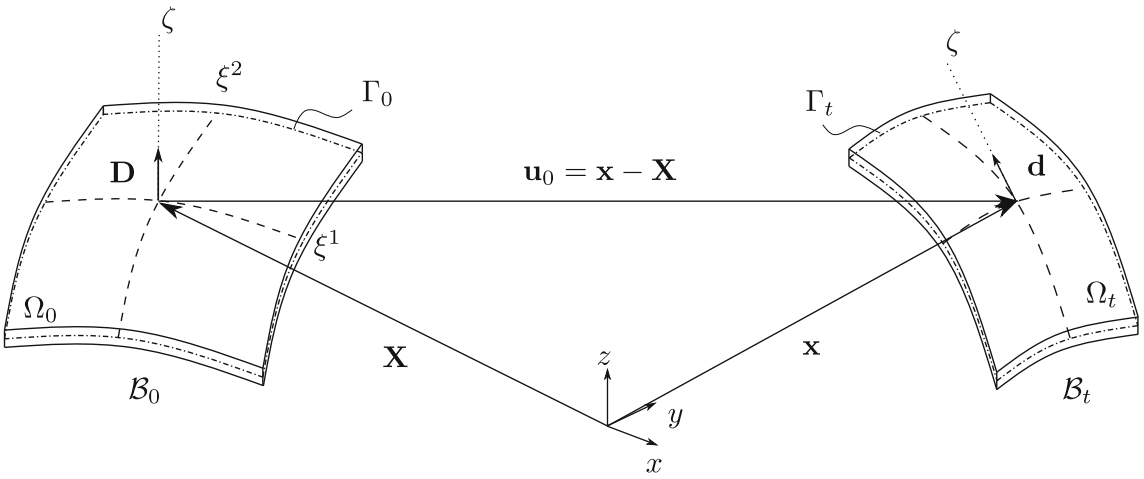

Fig. 1 Kinematic assumptions of a Reissner–Mindlin shell

$$\begin{bmatrix} E_{11} \\ E_{22} \\ 2E_{12} \\ 2E_{13} \\ 2E_{23} \end{bmatrix} = \underbrace{\begin{bmatrix} 1\,0\,0\,\zeta\,0\,0\,0\,0 \\ 0\,1\,0\,0\,\zeta\,0\,0\,0 \\ 0\,0\,1\,0\,0\,\zeta\,0\,0 \\ 0\,0\,0\,0\,0\,0\,1\,0 \\ 0\,0\,0\,0\,0\,0\,0\,1 \end{bmatrix}}_{\mathbf{A}(\zeta)} \begin{bmatrix} \varepsilon_{11} \\ \varepsilon_{22} \\ 2\varepsilon_{12} \\ \kappa_{11} \\ \kappa_{22} \\ 2\kappa_{12} \\ \gamma_1 \\ \gamma_2 \end{bmatrix}. \tag{5}$$

The shifter tensor $\mathbf{Z}$ is introduced, which relates the covariant basis to the local ortho-normal basis system. Its determinant $\mu = \det \mathbf{Z}$ is employed for the definition of a volume element $\mathrm{d}V = \mu \, \mathrm{d}\zeta \, \mathrm{d}A$. The internal virtual work can be defined as

$$\delta W_i = \int_{\Omega_0} \delta \boldsymbol{\varepsilon}^{\mathrm{T}} \boldsymbol{\sigma} \, \mathrm{d}A, \tag{6}$$

where

$$\delta \boldsymbol{\varepsilon} = \left[\delta\varepsilon_{11} \; \delta\varepsilon_{22} \; 2\delta\varepsilon_{12} \; \delta\kappa_{11} \; \delta\kappa_{22} \; 2\delta\kappa_{12} \; \delta\gamma_1 \; \delta\gamma_2\right]^{\mathrm{T}} \tag{7}$$

denotes the virtual shell strains. In analogy to Eq. 4, the virtual components are derived as

$$\begin{aligned} \delta\varepsilon_{\alpha\beta} &= \frac{1}{2}\left(\delta\mathbf{x}_{,\alpha} \cdot \mathbf{x}_{,\beta} + \delta\mathbf{x}_{,\beta} \cdot \mathbf{x}_{,\alpha}\right), \\ \delta\kappa_{\alpha\beta} &= \frac{1}{2}(\delta\mathbf{x}_{,\alpha} \cdot \mathbf{d}_{,\beta} + \delta\mathbf{x}_{,\beta} \cdot \mathbf{d}_{,\alpha} \\ &\quad + \delta\mathbf{d}_{,\alpha} \cdot \mathbf{x}_{,\beta} + \delta\mathbf{d}_{,\beta} \cdot \mathbf{x}_{,\alpha}), \\ \delta\gamma_\alpha &= \delta\mathbf{x}_{,\alpha} \cdot \mathbf{d} + \delta\mathbf{d} \cdot \mathbf{x}_{,\alpha}. \end{aligned} \tag{8}$$

$\boldsymbol{\sigma}$ in Eq. 6 denotes the vector of stress resultants, which is defined as $\boldsymbol{\sigma} = \left[n_{11} \; n_{22} \; n_{12} \; m_{11} \; m_{22} \; m_{12} \; q_1 \; q_2\right]^{\mathrm{T}}$. Here, $n_{\alpha\beta}$ are the membrane forces, $m_{\alpha\beta}$ the bending moments and q_α denote the shear forces.

Using the matrix $\mathbf{A}(\zeta)$ introduced in Eq. 5 the stress resultants can be related to the second Piola-Kirchhoff stress tensor $\mathbf{S}$,

$$\boldsymbol{\sigma} = \int_\zeta \mathbf{A}^{\mathrm{T}} \mathbf{S} \, \mu \, \mathrm{d}\zeta. \tag{9}$$

The weak form of equilibrium reads

$$\begin{aligned} g(\mathbf{v}, \delta\mathbf{v}) = &\int_{\Omega_0} \left(\delta\boldsymbol{\varepsilon}^{\mathrm{T}}\boldsymbol{\sigma} - \delta\mathbf{v}^{\mathrm{T}}\mathbf{p}\right) \mathrm{d}A \\ &- \int_{\Gamma_0} \delta\mathbf{v}^{\mathrm{T}}\mathbf{f} \, \mathrm{d}S = 0. \end{aligned} \tag{10}$$

The displacements $\mathbf{u}$ and the rotations $\boldsymbol{\omega}$ have been summarised in a vector $\mathbf{v} = \left[\mathbf{u} \; \boldsymbol{\omega}\right]^{\mathrm{T}}$. $\mathbf{p}$ denote surface loads and $\mathbf{f}$ are loads acting on the boundary of the shell's reference surface.

The Gâteaux derivative, needed for the linearization, reads

$$\mathrm{D}g(\mathbf{v}, \delta\mathbf{v}) \cdot \Delta\mathbf{v} = \int_{\Omega_0} \delta\boldsymbol{\varepsilon}^{\mathrm{T}} \mathbb{D} \Delta\boldsymbol{\varepsilon} + \Delta\delta\boldsymbol{\varepsilon}^{\mathrm{T}} \boldsymbol{\sigma} \, \mathrm{d}A, \tag{11}$$

where $\mathbb{D}$ denotes the shell material tangent operator. The linearised shell strains $\Delta\boldsymbol{\varepsilon}$ are derived similarly to Eq. 8. The derivation of the linearized virtual shell strains $\Delta\delta\boldsymbol{\varepsilon}$ can be found, for example, in [40].

3 Scaled boundary isogeometric analysis

The representative volume element (RVE) describing the mesostructure is analysed using the scaled boundary isogeometric analysis (SBIGA). In the following, a brief overview of the method will be given. For more detailed information on the method and its application to two- and three-dimensional problems, one is referred to previous works [5, 8].

Any domain in the reference configuration is denoted as Ω_0^{RVE} and can be divided into a number of n_{sec} sections $\Omega_{0,s}^{RVE}$. Each section is defined by its boundary surface $\Gamma_{0,s}^{RVE}$ parameterized by two parameters $0 \leq \eta, \zeta \leq 1$, compare Fig. 2. This boundary description can be obtained directly from CAD software in terms of Non-Uniform Rational B-Splines (NURBS). In a numerical context, the bi-variate NURBS basis functions will be adopted not only for the description of the geometry but also for the approximation of the displacement field. To obtain a three-dimensional geometry description, a scaling centre C is introduced. Special attention has to be paid when the scaling centre C is defined, as it must be visible from the entire boundary [32]. Here, star-shaped domains are obtained by manual subdivision. Algorithms for domain decomposition have been presented in e.g. [2]. The interior of the solid is described by the scaling parameter ξ, which runs from the scaling centre C ($\xi = 0$) to the boundary (ξ=1), see Fig. 2. The approximation of the displacements in the interior is based on uni-variate B-Splines.

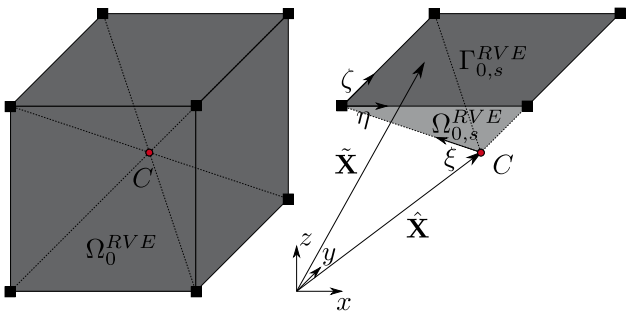

Fig. 2 The three-dimensional RVE domain Ω_0^{RVE} (left) and one exemplary section $\Omega_{0,s}^{RVE}$ (right)

Any point in the domain can be expressed as

$$\mathbf{X}(\xi,\eta,\zeta) = \hat{\mathbf{X}} + \xi\left(\tilde{\mathbf{X}}(\eta,\zeta) - \hat{\mathbf{X}}\right). \tag{12}$$

Where $\hat{\mathbf{X}}$ is the position vector of the scaling centre C and $\tilde{\mathbf{X}}$ describes any point on the boundary. Using the position vector of the boundary control points $\mathbf{X}_s$ and NURBS basis functions describing the boundary $\mathbf{N}_b(\eta,\zeta)$ one can write $\tilde{\mathbf{X}} = \mathbf{N}_b(\eta,\zeta)\,\mathbf{X}_s$.

The Jacobian is defined in a multiplicative manner as

$$\begin{aligned}\mathbf{J} &= \begin{bmatrix} \frac{\partial X_1}{\partial\xi} & \frac{\partial X_2}{\partial\xi} & \frac{\partial X_3}{\partial\xi} \\ \frac{\partial X_1}{\partial\eta} & \frac{\partial X_2}{\partial\eta} & \frac{\partial X_3}{\partial\eta} \\ \frac{\partial X_1}{\partial\zeta} & \frac{\partial X_2}{\partial\zeta} & \frac{\partial X_3}{\partial\zeta} \end{bmatrix} \\ &= \begin{bmatrix} 1 & 0 & 0 \\ 0 & \xi & 0 \\ 0 & 0 & \xi \end{bmatrix} \underbrace{\begin{bmatrix} \tilde{X}_1 - \hat{X}_1 & \tilde{X}_2 - \hat{X}_2 & \tilde{X}_3 - \hat{X}_3 \\ \frac{\partial \tilde{X}_1}{\partial\eta} & \frac{\partial \tilde{X}_2}{\partial\eta} & \frac{\partial \tilde{X}_3}{\partial\eta} \\ \frac{\partial \tilde{X}_1}{\partial\zeta} & \frac{\partial \tilde{X}_2}{\partial\zeta} & \frac{\partial \tilde{X}_3}{\partial\zeta} \end{bmatrix}}_{\bar{\mathbf{J}}(\eta,\zeta)}. \end{aligned} \tag{13}$$

Thus, a volume element $\mathrm{d}V$ in the physical space is defined as

$$\begin{aligned} \mathrm{d}V &= \det\mathbf{J}\,\mathrm{d}\xi\,\mathrm{d}\eta\,\mathrm{d}\zeta, \qquad \text{where} \\ \det\mathbf{J} &= \xi^2 \det\bar{\mathbf{J}}. \end{aligned} \tag{14}$$

The approximation of the displacement field $\mathbf{u}$ with NURBS basis functions, according to the concepts of isogeometric analysis, as well as the numerical treatment will be discussed in Sect. 5.2.

4 Basic principles of homogenization

The kinematics of the macroscopic and the mesoscopic scale have been introduced. The scales are connected by means of the Hill–Mandel condition which ensures energetic consistency. Figure 3 exemplary depicts the homogenization process. The macroscopic shell strains $\boldsymbol{\varepsilon}^M$ in each macroscopic integration point (denoted as 'GP') are applied to a mesoscopic representative volume element (RVE). The RVE height h always corresponds to the macroscopic shell thickness, which is one distinctive feature of the homogenization approach. On the mesoscopic scale, the boundary value problem ('BVP') on the RVE is solved and the homogenized shell stress resultants $\boldsymbol{\sigma}$ and the shell material tangent operator $\mathbb{D}$ are returned to the macroscopic scale.

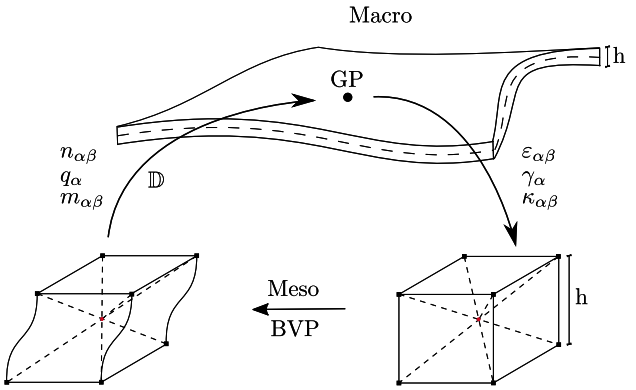

Fig. 3 First-order homogenization of a shell

4.1 Hill–Mandel condition

The aforementioned Hill–Mandel condition [24] requires the incremental energetic consistency between the two scales

$$\left\langle \mathbf{P}^m : \delta\mathbf{F}^m \right\rangle = \mathbf{P}^M : \delta\mathbf{F}^M. \tag{15}$$

Where the superscripts $(\bullet)^M$ and $(\bullet)^m$ denote the macro- and mesoscale, respectively. $\mathbf{P}$ denotes the first Piola Kirchhoff stress tensor and $\mathbf{F}$ the deformation gradient.

Generally, the macroscopic values are obtained from the mesoscopic volume average of the fields on the RVE. However, in shell theory, the macroscopic stress quantities are obtained by a through-thickness integration. Therefore, the brackets $\langle\bullet\rangle = \frac{1}{A^m}\int_{V^m}(\bullet)\,\mathrm{d}V$ indicate the mesoscopic work performed in an RVE per unit area of mid-surface [11].

Using Hill's lemma, Eq. 15 can be rewritten in terms of a surface integral over the RVE boundary, compare [35],

$$\begin{aligned} &\left\langle \mathbf{P}^m : \delta\mathbf{F}^m \right\rangle - \mathbf{P}^M : \delta\mathbf{F}^M \\ &= \frac{1}{A^m}\int_{\Gamma_0^{RVE}} (\mathbf{p}^m - \mathbf{P}^M\mathbf{N})(\delta\mathbf{x}^m - \delta\mathbf{F}^M\mathbf{X}^m)\,\mathrm{d}A. \end{aligned} \tag{16}$$

Where $\mathbf{p}^m$ denotes the stress vector and $\mathbf{N}$ is the corresponding normal vector of the surface. $\mathbf{x}^m$ and $\mathbf{X}^m$ are the position vectors in the current and reference configuration, respectively.

From Eq. 16 three types of boundary conditions can be derived.

1. Constant traction boundary conditions

$$\mathbf{p}^m = \mathbf{P}^M\mathbf{N} \quad \text{on} \quad \partial\Omega_0. \tag{17}$$

2. Linear displacement boundary conditions

$$\mathbf{x}^m = \mathbf{F}^M\mathbf{X}^m \quad \text{on} \quad \partial\Omega_0. \tag{18}$$

3. Periodic boundary conditions

$$\mathbf{x}^{m^+} - \mathbf{x}^{m^-} = \mathbf{F}^M(\mathbf{X}^{m^+} - \mathbf{X}^{m^-}) \quad \text{on} \quad \partial\Omega_0. \tag{19}$$

The periodic boundary conditions apply only for periodic mesostructures, i.e. the morphology repeats itself in close proximity to the macroscopic point. For a periodic RVE, the surface integral is divided into a positive, denoted by $(\bullet)^+$, and a negative side, denoted by $(\bullet)^-$, where the outward pointing unit normal vectors are equal and opposite on opposite sides. This implies that each point on the positive boundary can be uniquely related to a point on the negative boundary, therefore the opposing boundaries must be geometrically identical. Section 6 focuses on the chosen boundary conditions for the RVE.

4.2 Macro-Meso transition

One RVE occupies the space $[-l_x/2, l_x/2]\times[-l_y/2, l_y/2]\times[-h/2, h/2] \in \mathbb{R}^3$. For the top and bottom surfaces $z = \pm h/2$, zero-traction boundary conditions are applied. The macroscopic strains are applied via the lateral surfaces using boundary conditions fulfilling the Hill–Mandel condition. Note, that the RVE is defined in the ortho-normal basis system $\mathbf{e}_i$ with coordinates x, y, z while the shell is defined in the local ortho-normal basis system $\mathbf{A}_i$. The two coordinate systems are assumed to be equivalent. Thus, the indices of the shell quantities $\alpha, \beta = 1, 2$ in Sect. 2 are replaced by $\alpha, \beta = x, y$ without further consequences.

Assuming small strains, the linear displacement and periodic boundary conditions from the Hill–Mandel condition, following Eqs. 18 and 19, can be expressed by means of the Green-Lagrange strains. Thus, the relation between prescribed mesoscopic displacements, indicated by $(\bar{\bullet})$, of the lateral surfaces and the macroscopic strains can be written as

$$\begin{bmatrix}\bar{u}_x\\ \bar{u}_y\\ \bar{u}_z\end{bmatrix} = \begin{bmatrix}\varepsilon_{xx}+z\kappa_{xx} & \varepsilon_{xy}+z\kappa_{xy} & \frac{1}{2}\gamma_x\\ \varepsilon_{xy}+z\kappa_{xy} & \varepsilon_{yy}+z\kappa_{yy} & \frac{1}{2}\gamma_y\\ \frac{1}{2}\gamma_x & \frac{1}{2}\gamma_y & 0\end{bmatrix}\begin{bmatrix}x\\ y\\ z\end{bmatrix}. \tag{20}$$

The Green-Lagrange strains from Eq. 5 are expressed by the shell strains and written in matrix notation. Similar as in [21] displacements in thickness direction u_z are not prescribed, as for particular membrane and bending modes restraints are observed. Thus, Eq. 20 can be rewritten as

$$\begin{bmatrix}\bar{u}_x\\ \bar{u}_y\end{bmatrix} = \begin{bmatrix}\varepsilon_{xx}+z\kappa_{xx} & \varepsilon_{xy}+z\kappa_{xy} & \gamma_x\\ \varepsilon_{xy}+z\kappa_{xy} & \varepsilon_{yy}+z\kappa_{yy} & \gamma_y\end{bmatrix}\begin{bmatrix}x\\ y\\ z\end{bmatrix}. \tag{21}$$

Instead of prescribing the displacements for each control point, a rotation of the lateral surfaces can be prescribed to apply certain shell strains. For example, the curvature κ_{xx} in Fig. 4 can be either applied as a displacement, following Eq. 21,

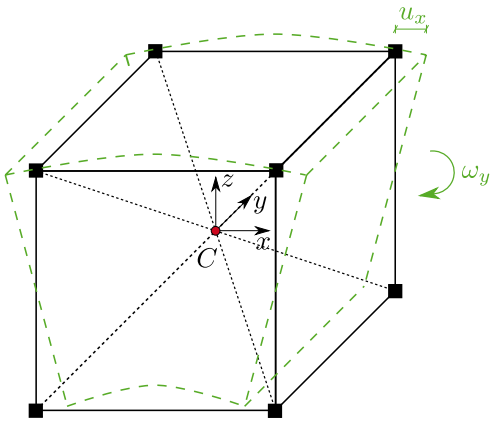

Fig. 4 Deformed RVE due to an applied κ_{xx}

$$\bar{u}_x = z\kappa_{xx}\, x \tag{22}$$

or as a rotation of the surface about the y-axis

$$\bar{\omega}_y = \frac{\partial \bar{u}_x}{\partial z} = \kappa_{xx}\, x. \tag{23}$$

To apply displacements and rotations to the lateral surfaces without explicitly prescribing control point displacements a transtion element, following [27], is employed. It introduces two additional control points for each lateral surface which describe the displacement and the rotation of the respective surface. Using Lagrange multipliers the deformation is enforced in an integral sense allowing the lateral surface to deform freely. The numerical treatment of the transition element will be presented in Sect. 5.3. Section 6 discusses for which of the in the following presented boundary conditions the transition element is used and the implications of its use on the deformation behaviour.

After the solution of the mesoscopic boundary value problem, the homogenized stress resultants $\boldsymbol{\sigma} = \begin{bmatrix} n_{xx} & n_{yy} & n_{xy} & m_{xx} & m_{yy} & m_{xy} & q_x & q_y\end{bmatrix}^{\mathrm{T}}$ and the shell material tangent operator $\mathbb{D}$ are returned to the macroscopic scale. For the linear-elastic, isotropic case Eq. 9 can be written as

$$\boldsymbol{\sigma} = \underbrace{\int_\zeta \mathbf{A}^{\mathrm{T}}\mathbb{C}\mathbf{A}\,\mu\,\mathrm{d}\zeta}_{\mathbb{D}}\,\boldsymbol{\varepsilon} = \begin{bmatrix}\mathbb{D}_m & \mathbb{D}_{mb} & 0\\ \mathbb{D}_{mb}^{\mathrm{T}} & \mathbb{D}_b & 0\\ 0 & 0 & \mathbb{D}_s\end{bmatrix}\boldsymbol{\varepsilon}, \tag{24}$$

where the indices denote membrane $(\bullet)_m$, bending $(\bullet)_b$ or shear $(\bullet)_s$ components, or a combination of these. $\mathbb{C}$ is

the continuum material tangent operator. For linear-elastic, isotropic material behaviour it reads

$$\mathbb{C} = \begin{bmatrix} \mathbb{C}_m^{3\times3} & \mathbf{0} \\ \mathbf{0} & \mathbb{C}_s^{2\times2} \end{bmatrix} = \frac{E}{1-\nu^2} \begin{bmatrix} 1 & \nu & 0 & 0 & 0 \\ \nu & 1 & 0 & 0 & 0 \\ 0 & 0 & \frac{1-\nu}{2} & 0 & 0 \\ 0 & 0 & 0 & \frac{1-\nu}{2} & 0 \\ 0 & 0 & 0 & 0 & \frac{1-\nu}{2} \end{bmatrix}. \tag{25}$$

When the mid-surface is used as reference surface, hence $z = 0$ when $-h/2 \leq z \leq h/2$, and the shell is assumed to be plane, the sub-matrices from Eq. 24 can be derived as

$$\begin{aligned} \mathbb{D}_m &= h\, \mathbb{C}_m, & \mathbb{D}_{mb} &= \mathbf{0}, \\ \mathbb{D}_b &= \frac{h^3}{12}\, \mathbb{C}_m, & \mathbb{D}_s &= \kappa\, h\, \mathbb{C}_s, \end{aligned} \tag{26}$$

where κ denotes the shear correction factor.

4.3 Shear inconsistency

As has been previously shown by e.g. [17] and [28] a kinematic inconsistency arises between the two scales for the transverse shears. In the following it will be presented for the shear strain γ_x, however, similar applies for the y-direction. From Eq. 21 follows a linear relationship between the displacement $\bar{u}_x$ and the shear strain γ_x,

$$\bar{u}_x = \gamma_x\, z. \tag{27}$$

Furthermore, from Eq. 24 the relation between shear force q_x and shear strain γ_x can be derived. For linear-elastic, isotropic material it reads

$$q_x = D_s^{11} \gamma_x = G h_s\, \gamma_x, \tag{28}$$

where G denotes the shear modulus and $h_s = h\,\kappa$. This is in contrast to the three-dimensional RVE, where generally an interaction between shear force and moments is observed. Similar as in [28] the two in-plane axes can be simplified individually as a fully clamped beam when prescribing displacements at the lateral surfaces, compare Fig. 5a. In this simplification, each axis is considered separately, thus no interaction between the two directions is taken into account. In addition, any boundary effects or lateral contraction are neglected.

Following Eq. 21 an applied transverse shear strain γ_x evokes a rotation of the clamped support. From beam analogy, it becomes obvious that a prescribed displacement evokes a linear moment distribution in addition to the constant shear distribution. The equivalent statical system and the force distributions are depicted in Fig. 5b. Furthermore, the transverse shear strain from shear contribution $\gamma_{x,S}$ and bending moment $\gamma_{x,b}$ are given for the beam. The shear force results from the addition of both components as

$$q_x = \underbrace{\left(\frac{12 E I\, G h_s}{(L^{RVE})^2 G h_s + 12 E I} \right)}_{(D_s^{11})^*} \gamma_x, \tag{29}$$

where $I = h^3/12$. Comparison of Eq. 28 and Eq. 29 illustrates the inconsistency $D_s^{11} \neq (D_s^{11})^*$. It can be seen that the RVE length L^{RVE} has a quadratic influence on the shear stiffness. Since L^{RVE} can be directly related to the bending moment distribution, compare Fig. 5b, the linear moment distribution has to be forced to zero using an additional constraint.

Enforcing

$$\begin{aligned} &\int_{L^{RVE}} m_{xx}\, x\, \mathrm{d}x = 0 \quad \text{and} \\ &\int_{L^{RVE}} m_{yy}\, y\, \mathrm{d}y = 0 \end{aligned} \tag{30}$$

the term $12EI/(L^{RVE})^2$ vanishes from Eq. 29 such that a consistent macro-to-meso-transition is possible. Assuming the principle of superposition, the constraints are two independent equations to remove (in homogeneous RVEs) or reduce (in general RVEs) the length dependency of the resulting shear stiffness on the length of the RVE. The numerical treatment of the additional constraint will be discussed in Sect. 5.4. Furthermore, an example to show the length dependent behaviour of the shear stiffness and the effect of the constraint is given in Appendix B. It is important to note, that the introduced additional constraints do not affect the proposed homogenization algorithm.

5 Finite element formulation

5.1 Shell element

The macroscopic shell is discretised using $e = 1, \ldots, numel$ isoparametric, quadrilateral shell elements [20]. The geometry and the displacements are approximated using bilinear shape functions

$$N_I(\xi^M, \eta^M) = \frac{1}{4}\left(1 + \xi_I\, \xi^M\right)\left(1 + \eta_I\, \eta^M\right) \quad \text{with} \quad \xi_I, \eta_I = \pm 1. \tag{31}$$

ξ^M, η^M denote the parameter space. The shape functions can be arranged in a shape function matrix $\mathbf{N}^M = \left[N_1\mathbf{I}, N_2\mathbf{I}, N_3\mathbf{I}, N_4\mathbf{I}\right]$. For plane shells, each node I has five

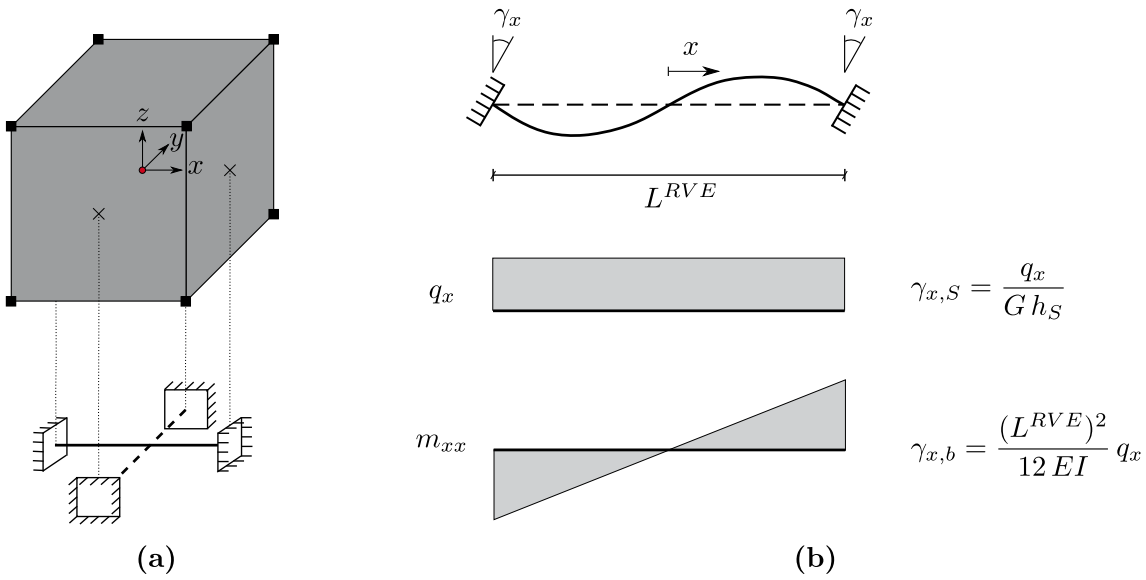

Fig. 5 **a** Beam analogy for an RVE **b** beam undergoing shear deformation, resulting shear force and bending moment distribution

nodal degrees of freedom, three displacements and two rotations, $\mathbf{v}_I = \left[u_x\ u_y\ u_z\ \omega_x\ \omega_y\right]_I^{\mathrm{T}}$. For intersections, the nodal degrees of freedom are extended by one additional rotation. To avoid shear locking a Bathe-Dvorkin [15] approach is used for the interpolation of the shear strains. The interpolation is inserted into the linearization of the system of equations which follows from Eqs. 10 and 11

$$L[g(\mathbf{v}^h, \delta\mathbf{v}^h), \Delta\mathbf{v}^h] = g(\mathbf{v}^h, \delta\mathbf{v}^h) + \mathrm{D}g(\mathbf{v}^h, \delta\mathbf{v}^h) \cdot \Delta\mathbf{v}^h = \sum_{e=1}^{numel} \delta\mathbf{v}_e^{\mathrm{T}} \left[\mathbf{f}_e + \mathbf{k}_e \Delta\mathbf{v}_e\right] = 0. \tag{32}$$

The tangential stiffness matrix and element residuum vector for the shell are defined as follows

$$\mathbf{k}_e = \int_{\Omega_{0,e}} \mathbf{B}^{\mathrm{T}} \mathbb{D} \mathbf{B} + \mathbf{G}\, \mathrm{d}A, \tag{33}$$

$$\mathbf{f}_e = \int_{\Omega_{0,e}} \mathbf{B}^{\mathrm{T}} \boldsymbol{\sigma} - \mathbf{N}^{M^{\mathrm{T}}} \mathbf{p}\, \mathrm{d}A - \int_{\Gamma_{0,e}} \mathbf{N}^{M^{\mathrm{T}}} \mathbf{f}\, \mathrm{d}S. \tag{34}$$

$\Omega_{0,e}$ denotes the shell reference surface for each element e and $\Gamma_{0,e}$ its boundary. The matrices $\mathbf{B}$ and $\mathbf{G}$ are specified in [40].

5.2 SB-IGA element

The implementation of the scaled boundary isogeometric element is briefly outlined in the following, for a more detailed description one is referred to [8]. Both, the geometry and the displacements are described using the same NURBS basis functions. These can be adopted from the CAD model describing the RVE and can be computed as shown in [33]. For the boundary they are independent of ξ and read $R_J^{p,q}(\eta, \zeta)$ for $J = 1, \ldots, n_{bc}$ boundary control points on $\Gamma_{0,s}^{RVE}$. They can be combined in matrix notation as

$$\mathbf{N}_b^{[3\times 3n_{bc}]}(\eta, \zeta) = \left[R_1^{p,q}\,\mathbf{I}, \ldots, R_{n_{bc}}^{p,q}\,\mathbf{I}\right]. \tag{35}$$

The dimension of the matrix is given as a superscript. It is $[3 \times 3\, n_{bc}]$ because three degrees of freedom are assumed for each control point. p and q denote the polynomial degree in the respective boundary direction. Similarly, the scaling direction ξ is approximated using B-Spline basis functions to allow for the solution of nonlinear problems [6]. They are denoted as $R_K^r(\xi)$, where r is the polynomial degree in scaling direction and index K ranges from 1 to n_{cp}. Here, n_{cp} is the number of control points along each scaling line, in total $n_{bs} = n_{cp} \cdot n_{bc}$ control points describe each section. The basis functions can be rewritten in matrix notation

$$\mathbf{N}_s^{[3n_{bc}\times 3n_{bs}]}(\xi) = \begin{bmatrix} R_1^r\,\mathbf{I} & \ldots & R_{n_{cp}}^r\,\mathbf{I} & \mathbf{0} & \ldots \\ \mathbf{0} & \ldots & \mathbf{0} & R_1^r\,\mathbf{I} & \ldots \\ \vdots & \ddots & \vdots & \vdots & \ddots \end{bmatrix}. \tag{36}$$

The consolidated shape function matrix for the mesoscale reads

$$\mathbf{N}^m(\eta, \zeta, \xi) = \mathbf{N}_b(\eta, \zeta)\mathbf{N}_s(\xi). \tag{37}$$

In the following the superscript $(\bullet)^m$ will be dropped for the sake of legibility. The shape function matrix can be used for the approximation of the displacements and the virtual displacements

$$\begin{aligned}\mathbf{u}^h &= \sum_{L=1}^{n_{bs}} N_L\,\mathbf{v}_L = \mathbf{N}\,\mathbf{v}_s,\\ \delta\mathbf{u}^h &= \sum_{L=1}^{n_{bs}} N_L\,\delta\mathbf{v}_L = \mathbf{N}\,\delta\mathbf{v}_s.\end{aligned} \tag{38}$$

Every control point has three degrees of freedom $\mathbf{v}_L = \left[u_x\ u_y\ u_z\right]_L^{\mathrm{T}}$ which can be assembled in a displacement vector for each section $\mathbf{v}_s$.

In accordance with [8] the discretised strain–displacement transformation matrix is written as

$$\begin{aligned}\mathbf{B} = \frac{1}{\det\bar{\mathbf{J}}}\Big(&\mathbf{b}_1\mathbf{N}_b\mathbf{N}_{s,\xi}\\ &+\frac{1}{\xi}\left(\mathbf{b}_2\mathbf{N}_{b,\eta}\mathbf{N}_s + \mathbf{b}_3\mathbf{N}_{b,\zeta}\mathbf{N}_s\right)\Big).\end{aligned} \tag{39}$$

Using Voigt notation it relates the deformation gradient $\mathbf{F}$ to the displacements via $\delta\mathbf{F} = \mathbf{B}\delta\mathbf{u}$. $(\bullet)_{,\xi}$ denotes the partial derivative with respect to ξ, similar applies for η and ζ. The matrices $\mathbf{b}_1$,$\mathbf{b}_2$ and $\mathbf{b}_3$ are dependent on the parameters η and ζ. The components are defined by the differential operator

$$\mathbf{D} = \mathbf{b}_1(\eta,\zeta)\frac{\partial}{\partial\xi} + \frac{1}{\xi}\left(\mathbf{b}_2(\eta,\zeta)\frac{\partial}{\partial\eta} + \mathbf{b}_3(\eta,\zeta)\frac{\partial}{\partial\zeta}\right) \tag{40}$$

and the inverse jacobian $\mathbf{J}^{-1}$, compare e.g. [8]. The Green-Lagrange strain and second Piola-Kirchoff stress tensor can be expressed in Voigt notation as $\mathbf{E}^{\mathrm{T}} = \left[E_{xx}\ \ E_{yy}\ \ E_{zz}\ \ 2E_{xy}\ \ 2E_{xz}\ \ 2E_{yz}\right]$ and $\mathbf{S}^{\mathrm{T}} = \left[S_{xx}\ S_{yy}\ S_{zz}\ S_{xy}\ S_{xz}\ S_{yz}\right]$. Following [8] a 6×9 matrix $\hat{\mathbf{F}}$ is defined, which contains the components of $\mathbf{F}$. Thus, the first variation of the Green-Lagrange strains can be written as $\delta\mathbf{E} = \hat{\mathbf{F}}\delta\mathbf{F}$. Consequently, the weak form of equilibrium can be expressed as

$$\begin{aligned}g\left(\mathbf{u}^h,\delta\mathbf{u}^h\right) = \sum_{s=1}^{n_{sec}}\delta\mathbf{v}_s^{\mathrm{T}}\Bigg[&\int_{\Omega_{0,s}^{RVE}}\mathbf{B}^{\mathrm{T}}\hat{\mathbf{F}}^{\mathrm{T}}\mathbf{S}\,\mathrm{d}V\\ &-\int_{\Omega_{0,s}^{RVE}}\mathbf{N}^{\mathrm{T}}\mathbf{b_0}\,\mathrm{d}V\\ &-\int_{\partial\Omega_{0,s}^{RVE}}\mathbf{N}^{\mathrm{T}}\mathbf{t_0}\mathrm{d}A\Bigg] = 0\\ = \sum_{s=1}^{n_{sec}}\delta\mathbf{v}_s^{\mathrm{T}}\,\mathbf{f}_s.&\end{aligned} \tag{41}$$

$\hat{\mathbf{F}}$ indicates the matrix notation of the deformation gradient, $\mathbf{S}$ denotes the second Piola-Kirchhoff stress tensor and $\mathbf{b}_0$ and $\mathbf{t}_0$ are the volume and surface loads acting on each section, respectively. Hence, $\mathbf{f}_s$ is the residuum vector per section.

Consequently, the Gâteaux derivative is obtained as

$$\mathrm{D}g\left(\mathbf{u}^h,\delta\mathbf{u}^h\right)\cdot\Delta\mathbf{u}^h = \sum_{s=1}^{n_{sec}}\delta\mathbf{v}_s^{\mathrm{T}}\,\mathbf{k}_s\,\Delta\mathbf{v}_s,$$

with

$$\mathbf{k}_s = \int_{\Omega_{0,s}^{RVE}}\xi^2\mathbf{B}^{\mathrm{T}}\left(\hat{\mathbf{F}}^{\mathrm{T}}\mathbb{C}\hat{\mathbf{F}} + \hat{\mathbf{S}}\right)\mathbf{B}\det\bar{\mathbf{J}}\,\mathrm{d}\xi\,\mathrm{d}\eta\,\mathrm{d}\zeta \tag{42}$$

where $\mathbb{C}$ is the consistent tangent modulus, $\mathbf{k}_s$ is the stiffness matrix per section s and $\hat{\mathbf{S}}$ is the second Piola-Kirchhoff stress tensor in matrix notation, see [8].

The RVE domain Ω_0^{RVE} is decomposed into a number of n_{sec} sections. The neighbouring boundary surfaces are assumed to have the same polynomial degree and boundary control points. For simplicity, the scaling direction is discretised in the same manner, such that $p_b = p_c$ and $n_b = n_c$ applies, if not explicitly stated otherwise. $p_b = p = q$ and $p_c = r$ describe the polynomial degree in each boundary and scaling direction, respectively, whereas n_b and n_c denote the number of elements in each boundary direction and scaling direction, respectively. This discretisation is called conforming. Non-conforming discretisations might be more efficient but would necessitate a coupling approach. This is out of the scope of this work, but different approaches have been discussed in the literature e.g. [1, 7, 14].

Here, standard Gauss quadrature is employed with $n_{GP} \geq (p+1)\times(q+1)\times(r+1)$ quadrature points in each direction. This integration rule is generally not able to integrate NURBS exactly, however, the induced error vanishes with refinement. Alternative integration rules are discussed, for example, in [26]. Different refinement techniques, such as knot insertion or order elevation can be employed, see [25]. The iterative Newton–Raphson scheme is employed to obtain the solution.

5.3 Transition element

An alternative to prescribing displacements on the RVE is the use of a transition element, following the approach in [27]. As has been briefly shown in Sect. 4.2 the macroscopic strains can be applied by prescribing the deformation of the lateral surface. Thus, a two-dimensional transition element is introduced which will coincide with the cross-section of the volume model of the RVE, such that $\mathbf{x}_V = \mathbf{x}_S$. The geometry of the transition element is indicated by a darker shading in Fig. 6. Here, $\mathbf{x}_V$ describes the geometry of the volume in the current configuration and $\mathbf{x}_S$ is the geometry of the transition element. The kinematics of the transition element can be uniquely described by means of a translation $\mathbf{u}_{S0}$ and a rotation $\boldsymbol{\omega}$, where the translation corresponds to a point $\mathbf{X}_{S0}$ which lies on the surface and on the reference plane of the volume. Thus, the current and the reference configuration are related via $\mathbf{x}_{S0} = \mathbf{X}_{S0} + \mathbf{u}_{S0}$. The vector $\mathbf{r}_0$ relates any point

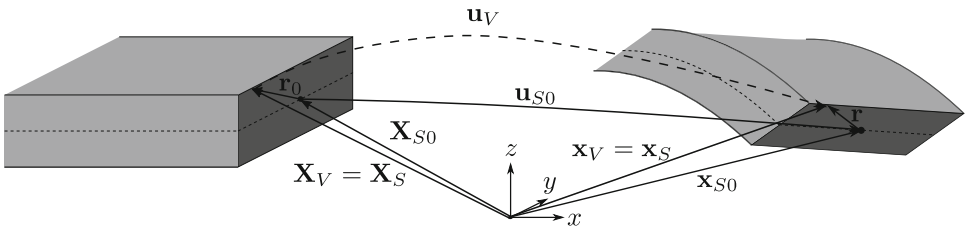

Fig. 6 Kinematic description of the transition element

$\mathbf{X}_V$ on the surface to the reference point $\mathbf{X}_{S0}$ in the reference configuration by $\mathbf{X}_V = \mathbf{X}_{S0} + \mathbf{r}_0$. Any point $\mathbf{x}_S$ on the surface in the current configuration reads

$$\begin{aligned} \mathbf{x}_S &= \mathbf{x}_{S0} + \mathbf{r} = \mathbf{X}_{S0} + \mathbf{u}_{S0} + \boldsymbol{\omega} \times \mathbf{r}_0 \\ &= \mathbf{x}_V = \mathbf{X}_V + \mathbf{u}_V, \end{aligned} \tag{43}$$

where $\mathbf{r} = \boldsymbol{\omega} \times \mathbf{r}_0$ is employed. It has to be noted, that while in the volume formulation each control point is assigned an individual displacement vector $\mathbf{u}_V$, the kinematics of the transition element depend on the translation $\mathbf{u}_{S0}$ and the rotation $\boldsymbol{\omega}$ only. $\mathbf{u}_{S0}$ and $\boldsymbol{\omega}$ are introduced as additional degrees of freedom together with two Lagrange parameters $\boldsymbol{\lambda}$ and $\boldsymbol{\mu}$. Thus, each transition element consists of $3 \times (n_{bc} + 4)$ degrees of freedom. The Lagrange parameter are used to enforce the geometric equivalence. The potential is extended by an additional term

$$\Pi = \cdots + \int_{\Gamma_0^{RVE}} \boldsymbol{\Lambda} \, (\mathbf{x}_V - \mathbf{x}_S) \, \mathrm{d}A = 0, \tag{44}$$

$$\text{where} \quad \boldsymbol{\Lambda} = \boldsymbol{\lambda} + \boldsymbol{\mu} \times \mathbf{r}_0. \tag{45}$$

In this case, the additional constraint is fulfilled in an integral sense. This means that the cross-section can deform freely while the constraint is fulfilled on average. Thus, the six Lagrange parameters, $\boldsymbol{\lambda}$ and $\boldsymbol{\mu}$, are chosen to be constant with regard to the cross-section. Fulfilling the constraint in a point-wise manner would result in the cross-section remaining plane after deformation. Using Eqs. 43 and 45, Eq. 44 can be rewritten as

$$\int_{\Gamma_0^{RVE}} (\boldsymbol{\lambda} + \boldsymbol{\mu} \times \mathbf{r}_0) \cdot (\mathbf{x}_V - \mathbf{X}_{S0} - \mathbf{u}_{S0} - \boldsymbol{\omega} \times \mathbf{r}_0) \, \mathrm{d}A. \tag{46}$$

The variation of the above yields the weak form of equilibrium as

$$\begin{aligned} g(\mathbf{u}, \delta\mathbf{u}) = \ldots \\ &+ \int_{\Gamma_0^{RVE}} \delta\mathbf{x}_V^T (\boldsymbol{\lambda} + \boldsymbol{\mu} \times \mathbf{r}_0) \\ &+ \delta\mathbf{u}_{S0}^T (-\boldsymbol{\lambda} - \boldsymbol{\mu} \times \mathbf{r}_0) \\ &+ \delta\boldsymbol{\omega}^T (\boldsymbol{\lambda} \times \mathbf{r}_0 + \mathbf{r}_0 \times (\mathbf{r}_0 \times \boldsymbol{\mu})) \\ &+ \delta\boldsymbol{\lambda}^T (\mathbf{x}_V - \mathbf{X}_{S0} - \mathbf{u}_{S0} - \boldsymbol{\omega} \times \mathbf{r}_0) \\ &+ \delta\boldsymbol{\mu}^T \mathbf{r}_0 \times (\mathbf{x}_V - \mathbf{X}_{S0} - \mathbf{u}_{S0} - \boldsymbol{\omega} \times \mathbf{r}_0) \, \mathrm{d}A = 0 \end{aligned} \tag{47}$$

and accordingly its Gâteaux derivative as

$$\begin{aligned} Dg(\mathbf{u}, \delta\mathbf{u}) \cdot \Delta\mathbf{u} = \ldots \\ &+ \int_{\Gamma_0^{RVE}} \delta\mathbf{x}_V^T (\Delta\boldsymbol{\lambda} - \mathbf{r}_0 \times \Delta\boldsymbol{\mu}) \\ &+ \delta\mathbf{u}_{S0}^T (-\Delta\boldsymbol{\lambda} + \mathbf{r}_0 \times \Delta\boldsymbol{\mu}) \\ &+ \delta\boldsymbol{\omega}^T (-\mathbf{r}_0 \times \Delta\boldsymbol{\lambda} + \mathbf{r}_0 \times (\mathbf{r}_0 \times \Delta\boldsymbol{\mu})) \\ &+ \delta\boldsymbol{\lambda}^T (\Delta\mathbf{x}_V - \Delta\mathbf{u}_{S0} + \mathbf{r}_0 \times \Delta\boldsymbol{\omega}) \\ &+ \delta\boldsymbol{\mu}^T \mathbf{r}_0 \times (\Delta\mathbf{x}_V - \Delta\mathbf{u}_{S0} + \mathbf{r}_0 \times \Delta\boldsymbol{\omega}) \, \mathrm{d}A. \end{aligned} \tag{48}$$

Where

$$\delta\mathbf{x}_V = \delta\mathbf{u}_V, \qquad \Delta\mathbf{x}_V = \Delta\mathbf{u}_V, \tag{49}$$

$$\delta\mathbf{x}_{S0} = \delta\mathbf{u}_{S0} \quad \text{and} \quad \Delta\mathbf{x}_{S0} = \Delta\mathbf{u}_{S0} \tag{50}$$

apply. The discretization of the transition element follows the one on the RVE surface. Thus, the stiffness matrix and element load vector have to be determined for each section on which the transition element is applied. To do so, the unknowns have to be approximated. The Lagrange parameters are chosen to be constant for each cross-section and are therefore constant for each element. Thus, the shape function is chosen to be 1. The additional degrees of freedom $\mathbf{u}_{S0}$ and $\boldsymbol{\omega}$ are approximated accordingly.

The remaining degrees of freedom $\mathbf{x}_V$, or $\mathbf{u}_V$, are approximated using the same NURBS shape functions, which are used to approximate the RVE-volume, see Eq. 37 with $\xi = 1$. Again, the superscript $(\bullet)^m$ is neglected in the following.

$$\begin{aligned} \mathbf{x}_V^h &= \sum_{J=1}^{n_{bc}} N_J \, \mathbf{x}_{VJ} = \sum_{J=1}^{n_{bc}} N_J (\mathbf{X}_{VJ} + \mathbf{v}_J) \\ \delta\mathbf{x}_V^h &= \sum_{J=1}^{nbc} N_J \delta\mathbf{x}_{VJ} = \sum_{J=1}^{nbc} N_J \delta\mathbf{v}_J \\ \Delta\mathbf{x}_V^h &= \sum_{J=1}^{nbc} N_J \Delta\mathbf{x}_{VJ} = \sum_{J=1}^{nbc} N_J \Delta\mathbf{v}_J \\ \mathbf{r}_0^h &= \sum_{J=1}^{nbc} N_J \mathbf{X}_{VJ} - \mathbf{X}_{S0} \end{aligned} \tag{51}$$

The superscript $(\bullet)^h$ indicates an approximated value, and the subscript $(\bullet)_J$ denotes a control point value and its corre-

sponding shape function N_J. n_{bc} is the number of boundary control points per transition element and corresponds to the boundary control points of the corresponding section. It has to be noted, that the additional nodes $\mathbf{u}_{S0}$, $\boldsymbol{\omega}$, $\boldsymbol{\lambda}$ and $\boldsymbol{\mu}$ do not count into n_{bc}.

Using this approximation one can arrive at the formulation of a load vector $\tilde{\mathbf{f}}_s$ and stiffness matrix $\tilde{\mathbf{k}}_s$ for each section

$$\begin{aligned}\tilde{\mathbf{f}}_s &= \begin{bmatrix}\mathbf{f}_a\\ \mathbf{f}_b\\ \mathbf{f}_c\\ \mathbf{f}_d\\ \mathbf{f}_e\end{bmatrix}\\ &= \int_{\Gamma_0^{RVE}} \begin{bmatrix}\mathbf{N}^{\mathrm{T}}(\boldsymbol{\lambda}+\boldsymbol{\mu}\times\mathbf{r}_0^h)\\ \mathbf{x}_V^h-\mathbf{X}_S-\mathbf{u}_{S0}-\boldsymbol{\omega}\times\mathbf{r}_0^h\\ \mathbf{r}_0^h(\mathbf{x}_V^h-\mathbf{X}_S-\mathbf{u}_{S0}-\boldsymbol{\omega}\times\mathbf{r}_0^h)\\ -\boldsymbol{\lambda}-\boldsymbol{\mu}\times\mathbf{r}_0^h\\ \boldsymbol{\lambda}\times\mathbf{r}_0^h+\mathbf{r}_0^h\times(\mathbf{r}_0^h\times\boldsymbol{\mu})\end{bmatrix}\mathrm{d}A, \end{aligned} \tag{52}$$

$$\begin{aligned}\tilde{\mathbf{k}}_s &= \begin{bmatrix}\mathbf{0} & \mathbf{k}_{ab} & \mathbf{k}_{ac} & \mathbf{0} & \mathbf{0}\\ \mathbf{k}_{ba} & \mathbf{0} & \mathbf{0} & \mathbf{k}_{bd} & \mathbf{k}_{be}\\ \mathbf{k}_{ca} & \mathbf{0} & \mathbf{0} & \mathbf{k}_{cd} & \mathbf{k}_{ce}\\ \mathbf{0} & \mathbf{k}_{db} & \mathbf{k}_{dc} & \mathbf{0} & \mathbf{0}\\ \mathbf{0} & \mathbf{k}_{eb} & \mathbf{k}_{ec} & \mathbf{0} & \mathbf{0}\end{bmatrix}\\ &= \int_{\Gamma_0^{RVE}} \begin{bmatrix}\mathbf{0} & \mathbf{N}^{\mathrm{T}}\mathbf{1} & \mathbf{N}^{\mathrm{T}}[\mathbf{r}_0^h]_\times^{\mathrm{T}} & \mathbf{0} & \mathbf{0}\\ \mathbf{1N} & \mathbf{0} & \mathbf{0} & -\mathbf{1} & [\mathbf{r}_0^h]_\times\\ [\mathbf{r}_0^h]_\times\mathbf{N} & \mathbf{0} & \mathbf{0} & [\mathbf{r}_0^h]_\times^{\mathrm{T}} & [\mathbf{r}_0^h]_\times[\mathbf{r}_0^h]_\times\\ \mathbf{0} & -\mathbf{1} & [\mathbf{r}_0^h]_\times & \mathbf{0} & \mathbf{0}\\ \mathbf{0} & [\mathbf{r}_0^h]_\times^{\mathrm{T}} & [\mathbf{r}_0^h]_\times[\mathbf{r}_0^h]_\times & \mathbf{0} & \mathbf{0}\end{bmatrix}\mathrm{d}A. \end{aligned} \tag{53}$$

The integral is applied component-wise and $[\bullet]_\times$ is used to denote the skew-symmetric matrix of a vector, which is defined as

$$[\mathbf{a}]_\times = \begin{bmatrix}0 & -a_3 & a_2\\ a_3 & 0 & -a_1\\ -a_2 & a_1 & 0\end{bmatrix}. \tag{54}$$

The diagonal entries of the stiffness matrix $\tilde{\mathbf{k}}_s$ are zero, which indicates that the problem is indefinite, due to the enforcement of the additional constraint using Lagrange parameters.

To account for stiffness jumps within heterogeneous cross-sections the stiffness matrix and load vector are scaled. Under the assumption of linear-elastic material behaviour and small deformations of the transition element, it is sufficient to consider only the stiffness relating to the normal direction for scaling purposes. Thus, for the x-direction scaling is carried out using the entry $C_{11} = \dfrac{E}{1-\nu^2}$. Similarly, transition elements whose normal vector points in the y-direction are scaled by C_{22}. This procedure evokes jumps in the normal stress distribution and allows for a uniform boundary deformation. In Fig. 7 the normal stress distribution is exemplary given for a three-layered RVE with a softer core. Here, the Lagrange parameters can be interpreted as strain in longitudinal direction λ_x and a curvature μ_y about the y-axis. The assumption of constant Lagrange multipliers for each cross-section is relaxed so that they only have to be element-wise constant. The stiffness matrix and force vector are thus defined as follows

$$\mathbf{k}_s = C_{11}\tilde{\mathbf{k}}_s, \qquad \mathbf{f}_s = C_{11}\tilde{\mathbf{f}}_s. \tag{55}$$

5.4 Moment reduction constraint

In this section, a volume element is introduced in order to apply the additional constraint introduced in Sect. 4.3, following the approach in [28]. The moment distribution due to the applied shear deformation will be enforced to be zero. From the beam analogy discussed in Sect. 4.3 results a linear moment distribution over the RVE, compare Fig. 5. The additional volume elements coincide with the volume elements used to discretise the RVE. Therefore, scaled boundary isogeometric analysis is adopted for these elements also. Again, linear elastic material behaviour and small deformations are assumed for this internal constraint. It can be written as

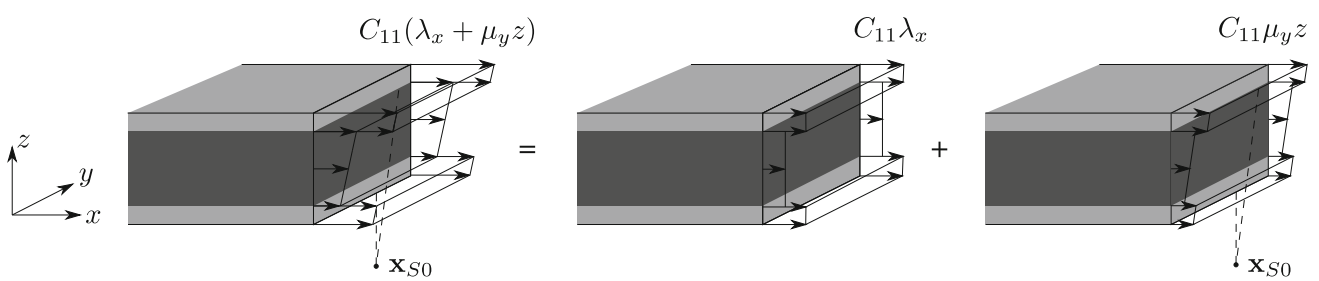

Fig. 7 Normal stress distribution for a layered RVE with softer core

$$\int_{L_0^{RVE}} \int_{\Gamma_0^{RVE}} \sigma_x(\lambda_x + \mu_y \cdot z)\mathrm{d}A\ \mathrm{d}L = \int_{\Omega_0^{RVE}} \sigma_x(\lambda_x + \mu_y \cdot z)\mathrm{d}V = 0, \tag{56}$$

where σ_x describes the x-component of the stress. The same applies for the component σ_y, here we restrict ourselves to the derivation for σ_x.

Similar to Sect. 5.3 the formulation of the potential can be extended by one additional term.

$$\Pi = \cdots + \int_{\Omega_0^{RVE}} \sigma_x(\lambda_x + \mu_y \cdot z)\mathrm{d}V = \cdots + \int_{\Omega_0^{RVE}} \sigma_x \overline{\mathbf{p}} \cdot \mathbf{\Lambda}\mathrm{d}V = 0 \tag{57}$$

The equation has been simplified using the position vector $\overline{\mathbf{p}} = \begin{bmatrix}1 & z\end{bmatrix}^{\mathrm{T}}$ and the Lagrange parameters $\mathbf{\Lambda} = \begin{bmatrix}\lambda_x & \mu_y\end{bmatrix}^{\mathrm{T}}$. The first variation is added to the weak form of equilibrium

$$g(\mathbf{u}, \delta\mathbf{u}) = \cdots + \int_{\Omega_0^{RVE}} (\delta\sigma_x \overline{\mathbf{p}} \cdot \mathbf{\Lambda} + \sigma_x \overline{\mathbf{p}} \cdot \delta\mathbf{\Lambda})\,\mathrm{d}V. \tag{58}$$

The Gâteaux derivative follows as

$$Dg(\mathbf{u}, \delta\mathbf{u}) \cdot \Delta\mathbf{u} = \ldots + \int_{\Omega_0^{RVE}} (\delta\sigma_x \overline{\mathbf{p}} \cdot \Delta\mathbf{\Lambda} + \Delta\sigma_x \overline{\mathbf{p}} \cdot \delta\mathbf{\Lambda})\,\mathrm{d}V. \tag{59}$$

Assuming linear-elastic material behaviour of the additional volume element the stress in x-direction can be rewritten using $\boldsymbol{\sigma} = \mathbb{C} : \boldsymbol{\varepsilon}$ as

$$\sigma_x = \overline{\mathbb{C}}\,\boldsymbol{\varepsilon} = \sum_{s}^{n_{sec}} \sum_{L}^{n_{bs}} \overline{\mathbb{C}}\mathbf{B}_L \mathbf{v}_L. \tag{60}$$

The index L denotes each of the n_{bs} control points of each section n_{sec} of the domain. $\overline{(\bullet)}$ indicates the use of the first row of the material tangent $\mathbb{C}$ in Voigt Notation $\overline{\mathbb{C}} = \begin{bmatrix}C_{11} & C_{12} & C_{13} & C_{14} & C_{15} & C_{16}\end{bmatrix}$. For the approximation of the displacements $\mathbf{v}_L = \begin{bmatrix}u_x & u_y & u_z\end{bmatrix}_L^{\mathrm{T}}$ the same shape functions, as the ones used for approximation of the volume of the RVE are used, see Eq. 37. The Lagrange parameters are approximated with shape functions analogously to the resulting moment distribution. Again, with reference to beam analogy in Sect. 4.3, a linear moment distribution is assumed, therefore

$$N_\Lambda = x. \tag{61}$$

Using Eq. 58 the element load vector reads

$$\int_{\Omega_0^{RVE}} (\delta\sigma_x \overline{\mathbf{p}} \cdot \mathbf{\Lambda} + \sigma_x \overline{\mathbf{p}} \cdot \delta\mathbf{\Lambda})\mathrm{d}V = \sum_{s=1}^{n_{sec}} \begin{bmatrix}\delta\mathbf{v}_s \\ \delta\mathbf{\Lambda}_s\end{bmatrix}^{\mathrm{T}} \underbrace{\begin{bmatrix}\int_{\Omega_0^{RVE}} \mathbf{B}^{\mathrm{T}}\overline{\mathbb{C}}^{\mathrm{T}}\overline{\mathbf{p}} \cdot\ \mathbf{\Lambda}_s\ \mathrm{d}V \\ \int_{\Omega_0^{RVE}} \overline{\mathbf{p}}\,\overline{\mathbb{C}}\,\mathbf{B}\,\mathbf{v}_s\ \mathrm{d}V\end{bmatrix}}_{\mathbf{f}_s}. \tag{62}$$

From the linearization, Eq. 59, the element stiffness matrix can be derived. Similar to the stiffness matrix of the transition element it has a zero diagonal,

$$\int_{\Omega_0^{RVE}} (\delta\sigma_x \overline{\mathbf{p}} \cdot \Delta\mathbf{\Lambda} + \Delta\sigma_x \overline{\mathbf{p}} \cdot \delta\mathbf{\Lambda})\mathrm{d}V = \sum_{s=1}^{n_{sec}} \begin{bmatrix}\delta\mathbf{v}_s \\ \delta\mathbf{\Lambda}_s\end{bmatrix}^{\mathrm{T}} \underbrace{\begin{bmatrix}0 & \mathbf{k}_{ab} \\ \mathbf{k}_{ab}^{\mathrm{T}} & 0\end{bmatrix}}_{\mathbf{k}_s} \begin{bmatrix}\Delta\mathbf{v}_s \\ \Delta\mathbf{\Lambda}_s\end{bmatrix}, \tag{63}$$

where

$$\mathbf{k}_{ab} = \int_{\Omega_0^{RVE}} \mathbf{B}^{\mathrm{T}}\overline{\mathbb{C}}^{\mathrm{T}}\overline{\mathbf{p}}^{\mathrm{T}}\mathbf{N}_\Lambda \mathrm{d}V. \tag{64}$$

5.5 Micro–Macro transition

The homogenization algorithm follows the approach in [21]. To obtain the linearization of the weak form of the coupled problem the weak forms and their derivatives for both scales are combined. To each macroscopic integration point $i = 1, \ldots, nGP$ in every macroscopic element $e = 1, \ldots, numel$ an RVE is assigned. External loads are acting exclusively on the macroscopic scale, therefore the load terms from Eq. 41 are omitted. The linearization reads

$$\begin{aligned} L[G(\mathbf{v}, \delta\mathbf{v}), \Delta\mathbf{v}] &= \int_\Omega \delta\boldsymbol{\varepsilon}^{M\mathrm{T}}\boldsymbol{\sigma}^M\,\mathrm{d}A + \{\text{external loads}\} \\ &+ \int_\Omega \delta\boldsymbol{\varepsilon}^{M\mathrm{T}}\mathbb{D}\Delta\boldsymbol{\varepsilon}^M + \Delta\delta\boldsymbol{\varepsilon}^{M\mathrm{T}}\boldsymbol{\sigma}^M\,\mathrm{d}A \\ &+ \sum_{e=1}^{numel}\sum_{i=1}^{nGP}\left[\frac{1}{A_i}\left(\int_{\Omega_{0,i}^{RVE}} \delta\mathbf{E}^{\mathrm{T}}\mathbf{S}\,\mathrm{d}V \right.\right. \\ &\left.\left. + \int_{\Omega_{0,i}^{RVE}} \delta\mathbf{E}^{\mathrm{T}}\mathbb{C}\Delta\mathbf{E} + \Delta\delta\mathbf{E}^{T}\mathbf{S}\,\mathrm{d}V\right)\right]. \end{aligned} \tag{65}$$

Here, the superscript $(\bullet)^M$ indicates a macroscopic quantity, for simplicity no superscript for mesoscopic quantities is used. Integration on the mesoscale is carried out over the RVE volume and averaged over the area of the RVE mid-surface A_i, see Sect. 4.1. Using Lagrange polynomials and NURBS

functions for approximation on the macro- and mesoscale, respectively, the following system of equations is obtained

$$
\begin{aligned}
&L[G(\mathbf{v}^h, \delta\mathbf{v}^h), \Delta\mathbf{v}^h] \\
&= \sum_{e=1}^{numel} \begin{bmatrix} \delta\mathbf{v}^M \\ \delta\mathbf{V}_1 \\ \vdots \\ \delta\mathbf{V}_{nGP} \end{bmatrix}_e^{\mathrm{T}} \\
&\left\{ \begin{bmatrix} \mathbf{k}^M(\mathbb{D}_i) & \mathbf{0} & \dots & \mathbf{0} \\ \mathbf{0} & \mathbf{K}_1 & \dots & \mathbf{0} \\ \vdots & \vdots & \ddots & \vdots \\ \mathbf{0} & \mathbf{0} & \dots & \mathbf{K}_{nGP} \end{bmatrix} \begin{bmatrix} \Delta\mathbf{v}^M \\ \Delta\mathbf{V}_1 \\ \vdots \\ \Delta\mathbf{V}_{nGP} \end{bmatrix} \right. \\
&\left. + \begin{bmatrix} \mathbf{f}^M(\boldsymbol{\sigma}_i) \\ \mathbf{F}_1 \\ \vdots \\ \mathbf{F}_{nGP} \end{bmatrix} \right\}_e = 0.
\end{aligned} \tag{66}
$$

The first row refers to the macroscopic boundary value problem while all others refer to one boundary value problem on the mesoscopic scale. Investigation of one mesoscopic boundary value problem for Gauss point i yields

$$
\delta\mathbf{V}_i^{\mathrm{T}} \left(\mathbf{K}_i \, \Delta\mathbf{V}_i + \mathbf{F}_i\right) = \frac{1}{A_i} \sum_{s=1}^{nsec} \delta\mathbf{v}_s^{\mathrm{T}} \left(\mathbf{k}_s \Delta\mathbf{v}_s + \mathbf{f}_s\right), \tag{67}
$$

where $\mathbf{f}_s$ and $\mathbf{k}_s$ are the load vector and stiffness matrix per section from Eq. 41 and Eq. 42, respectively. $nsec$ denotes the total number of sections describing the RVE. The mesoscopic displacement $\mathbf{v}_s$ is rearranged into a vector $\mathbf{v}_a$, which contains the internal displacements, and a vector $\mathbf{v}_b$ containing all boundary displacements. These are coupled to the macroscopic scale using the standard assembly matrix $\mathbf{a}_s$ to relate $\mathbf{v}_a$ to the macroscopic displacement vector $\mathbf{V}_i$. The boundary displacements are prescribed in each integration point i by the corresponding shell strains $\boldsymbol{\varepsilon}_i^M$. This relation is determined through a relational matrix $\mathbf{A}_s(x, y, z)$, which will be further specified in the following section

$$
\mathbf{v}_s = \begin{bmatrix} \mathbf{v}_a \\ \mathbf{v}_b \end{bmatrix} = \begin{bmatrix} \mathbf{a}_s \mathbf{V}_i \\ \mathbf{A}_s \boldsymbol{\varepsilon}_i^M \end{bmatrix}, \tag{68}
$$

The virtual and linearized relations are derived accordingly. $\mathbf{k}_{\alpha\beta}$ and $\mathbf{f}_\alpha$ with $\alpha, \beta = a, b$ are introduced as submatrices of $\mathbf{k}_s$ and $\mathbf{f}_s$. Consequently, Eq. 67 can be written as

$$
\begin{aligned}
&\delta\mathbf{V}_i^{\mathrm{T}} \left(\mathbf{K}_i \, \Delta\mathbf{V}_i + \mathbf{F}_i\right) \\
&= \frac{1}{A_i} \sum_{s=1}^{nsec} \begin{bmatrix} \delta\mathbf{V}_i \\ \delta\boldsymbol{\varepsilon}_i^M \end{bmatrix}^{\mathrm{T}} \\
&\left\{ \begin{bmatrix} \mathbf{a}_s^{\mathrm{T}}\mathbf{k}_{aa}\mathbf{a}_s & \mathbf{a}_s^{\mathrm{T}}\mathbf{k}_{ab}\mathbf{A}_s \\ \mathbf{A}_s^{\mathrm{T}}\mathbf{k}_{ba}\mathbf{a}_s & \mathbf{A}_s^{\mathrm{T}}\mathbf{k}_{bb}\mathbf{A}_s \end{bmatrix}_s \begin{bmatrix} \Delta\mathbf{V}_i \\ \Delta\boldsymbol{\varepsilon}_i^M \end{bmatrix} + \begin{bmatrix} \mathbf{a}_s^{\mathrm{T}}\mathbf{f}_a \\ \mathbf{A}_s^{\mathrm{T}}\mathbf{f}_b \end{bmatrix}_s \right\} \\
&= \frac{1}{A_i} \begin{bmatrix} \delta\mathbf{V}_i \\ \delta\boldsymbol{\varepsilon}_i^M \end{bmatrix}^{\mathrm{T}} \left\{ \begin{bmatrix} \mathbf{K} & \mathbf{L} \\ \mathbf{L}^{\mathrm{T}} & \mathbf{M} \end{bmatrix} \begin{bmatrix} \Delta\mathbf{V}_i \\ \Delta\boldsymbol{\varepsilon}_i^M \end{bmatrix} + \begin{bmatrix} \mathbf{F}_a \\ \mathbf{F}_b \end{bmatrix} \right\}
\end{aligned} \tag{69}
$$

Static condensation of the internal degrees of freedom can be conducted by

$$
\Delta\mathbf{V}_i = -\mathbf{K}^{-1} \left(\mathbf{L} \, \Delta\boldsymbol{\varepsilon}_i^M + \mathbf{F}_a\right), \tag{70}
$$

when $\delta\mathbf{V}_i \neq 0$ and rigid body motions are eliminated by appropriate boundary conditions, such that $\mathbf{K}^{-1}$ exists. Using Eq. 70, Eq. 69 can be rewritten as

$$
\begin{aligned}
&\delta\mathbf{V}_i^{\mathrm{T}} \left(\mathbf{K}_i \, \Delta\mathbf{V}_i + \mathbf{F}_i\right) \\
&= \frac{1}{A_i} \delta\boldsymbol{\varepsilon}_i^{M^{\mathrm{T}}} \left[\left(\mathbf{M} - \mathbf{L}^{\mathrm{T}}\mathbf{K}^{-1}\mathbf{L}\right) \Delta\boldsymbol{\varepsilon}_i^{M^{\mathrm{T}}} \right. \\
&\quad \left. + \left(\mathbf{F}_b - \mathbf{L}^{\mathrm{T}}\mathbf{K}^{-1}\mathbf{F}_a\right) \right] \\
&= \delta\boldsymbol{\varepsilon}_i^{M^{\mathrm{T}}} \left(\mathbb{D}_i \Delta\boldsymbol{\varepsilon}_i^M + \boldsymbol{\sigma}_i\right).
\end{aligned} \tag{71}
$$

Where the stress resultants and the macroscopic shell material tangent are introduced as

$$
\boldsymbol{\sigma}_i = \frac{1}{A_i} \left(\mathbf{F}_b - \mathbf{L}^{\mathrm{T}}\mathbf{K}^{-1}\mathbf{F}_a\right) \text{ and} \tag{72}
$$

$$
\mathbb{D}_i = \frac{1}{A_i} \left(\mathbf{M} - \mathbf{L}^{\mathrm{T}}\mathbf{K}^{-1}\mathbf{L}\right). \tag{73}
$$

Application of Eq. 71 to Eq. 66 leads to a consistently linearized homogenization scheme. The mesoscopic contributions $\mathbb{D}_i$ and $\boldsymbol{\sigma}_i$ for each integration point enter the macroscopic scale through $\mathbf{K}^M(\mathbb{D}_i)$ and $\mathbf{f}^M(\boldsymbol{\sigma}_i)$.

6 Boundary conditions of the representative volume element

In this section, three sets of boundary conditions for the lateral surfaces of the RVE will be specified. For the top and bottom face, at $z = \pm h/2$, zero-traction boundary conditions apply. The xy-plane always corresponds to the reference shell surface, where l_x and l_y denote the in-plane dimensions. These can generally be chosen independently. However, here $l_x = l_y$ is chosen for demonstrative purposes. In the following, the in-plane dimensions are denoted as L^{RVE}, where

$L^{RVE} = l_x = l_y$ applies. As has been derived in Sect. 4.1, generally three types of boundary conditions evolve from the Hill–Mandel equation. From Eq. 20 follows a relation which relates the lateral displacements for every control point to the macroscopic shell strains $\boldsymbol{\varepsilon}^M$ by means of a relational matrix $\mathbf{A}_J(x, y, z)$

$$\bar{\mathbf{u}}_J = \mathbf{A}_J(x, y, z)\, \boldsymbol{\varepsilon}^M. \tag{74}$$

The matrices $\mathbf{A}_J(x, y, z)$ refer to control points J of the considered section s and are submatrices of $\mathbf{A}_s$, see Eq. 68. Here, the matrix $\mathbf{A}_s$ is split into a geometric part $\tilde{\mathbf{A}}_s$ and a part for the transition element, from Sect. 5.3, $\hat{\mathbf{A}}_s$, such that

$$\mathbf{A}_s = \left[\tilde{\mathbf{A}}_s^{\mathrm{T}}\, \hat{\mathbf{A}}_s^{\mathrm{T}}\right]^{\mathrm{T}}. \tag{75}$$

Depending on the type of boundary condition, either part may vanish. The matrix $\tilde{\mathbf{A}}_s$ is specified as

$$\tilde{\mathbf{A}}_s = \begin{bmatrix} \delta_1 \tilde{\mathbf{A}}_1 \\ \vdots \\ \delta_J \tilde{\mathbf{A}}_J \\ \vdots \\ \delta_{n_{bs}} \tilde{\mathbf{A}}_{n_{bs}} \end{bmatrix} \quad \text{with} \qquad \delta_J = \begin{cases} 1 \text{ if control point } J \text{ has fixed DOFs} \\ 0 \text{ else} \end{cases}. \tag{76}$$

Where n_{bs} is the number of total control points per section. Accordingly, the matrix for the transition element reads

$$\hat{\mathbf{A}}_s = \begin{bmatrix} \delta_1 \hat{\mathbf{A}}_1 \\ \vdots \\ \delta_I \hat{\mathbf{A}}_I \\ \vdots \\ \delta_{ntrans} \hat{\mathbf{A}}_{ntrans} \end{bmatrix} \quad \text{with} \qquad \delta_j = \begin{cases} 1 \text{ if transition element } I \text{ has fixed DOFs} \\ 0 \text{ else} \end{cases}. \tag{77}$$

ntrans denotes the number of used transition elements in the formulation of the boundary conditions.

To avoid rigid body movements an arbitrary node is fixed in the z-direction for all sets of boundary conditions. The presented moment reduction constraint from Sect. 5.4 is applied for all three types of boundary conditions to reduce the length dependency of the shear stiffness. The necessity of the condition in terms of homogenization of shell structures was shown in [30].

6.1 Traction boundary conditions

One possibility to apply the shell strains to the RVE is the use of the presented transition element from Sect. 5.3. The translation $\mathbf{u}_{S0}$ and the rotation $\boldsymbol{\omega}$ of the transition element are prescribed which implicitly evoke the deformation of the RVE. Furthermore, the enforcement using Lagrange parameters causes constant tractions on the boundaries, which is shown in Sect. 6.4. Thus, in the following, this type of boundary conditions will be referred to as 'traction boundary conditions' (*tbc*). Note, that this formulation contradicts the 'classical' traction boundary conditions from Eq. 17, as no actual stresses are applied. A plane view of an RVE is depicted in Fig. 8. The dashed lines indicate the use of the transition element on all four faces. The translations u_{S0x} and u_{S0y} are prescribed for each lateral surface, while for each transition element only the in-plane rotation is prescribed. The out-of-plane rotation is linked to the opposing transition element, indicated by a dotted arrow and by the superscript $(\bullet)^{\parallel}$. Note, that in-plane rotation refers to the rotation about the in-plane axis but evokes and out of plane displacement. Because all macroscopic shell strains $\boldsymbol{\varepsilon}^M$ are applied using the transition element Eq. 75 can be written as $\mathbf{A}_s = \hat{\mathbf{A}}_s$. For each interface I the relation reads

$$\begin{bmatrix} \bar{u}_{S0x} \\ \bar{u}_{S0y} \\ \bar{\omega}_x \\ \bar{\omega}_y \end{bmatrix}_I = \underbrace{\begin{bmatrix} x & 0 & \frac{1}{2}y & 0 & 0 & 0 & 0 & 0 \\ 0 & y & \frac{1}{2}x & 0 & 0 & 0 & 0 & 0 \\ 0 & 0 & 0 & 0 & -y & -\frac{1}{2}x & 0 & -1 \\ 0 & 0 & 0 & x & 0 & \frac{1}{2}y & 1 & 0 \end{bmatrix}}_{\mathbf{A}_I^{tbc}} \boldsymbol{\varepsilon}^M. \tag{78}$$

6.2 Shell boundary conditions

The set of boundary conditions which will be referred to as 'shell boundary conditions' (*sbc*) in the following have been adapted from [21]. Similarly, the out-of-plane displace-

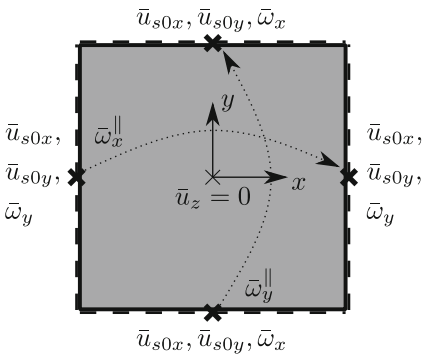

Fig. 8 Plane view of RVE-tbc: Displacements of transition element prescribed, in-plane rotation prescribed and out-of-plane rotation linked

ments of the RVE are fixed. However, in contrast to [21] the in-plane displacements are linked symmetrically. This adaption has become necessary when investigating problems, where the inhomogeneities do not span the whole width of the RVE. Exemplary, an RVE with circular inclusion is deformed by a macroscopic strain $\varepsilon^M_{yy} = 0.2$. Linear elastic material behaviour is assumed, where the inclusion is 100 times stiffer than the surrounding matrix material. Prescribing the in-plane displacements leads to unphysical deformations, see Fig. 9b. Relaxing the constraint by linking the in-plane displacements solves that problem, refer to Fig. 9c. Analogous to [21] the vertical displacement u_z is linked in an anti-symmetric way with respect to the x and y coordinates, denoted by the superscript $(\bullet)^\times$. For the present type of boundary condition, the transition element is not used. Therefore, Eq. 75 is simplified as $\mathbf{A}_s = \tilde{\mathbf{A}}_s$. It reads

$$\begin{bmatrix} \bar{u}_x \\ \bar{u}_y \end{bmatrix}_J = \underbrace{\begin{bmatrix} x & 0 & \frac{1}{2}y & x\,z & 0 & \frac{1}{2}y\,z & z & 0 \\ 0 & y & \frac{1}{2}x & 0 & y\,z & \frac{1}{2}x\,z & 0 & z \end{bmatrix}}_{\mathbf{A}^{sbc}_J} \boldsymbol{\varepsilon}^M. \tag{79}$$

Table 1 gives an overview of the applied boundary and linking conditions. Additionally, the plane view of the RVE in Fig. 10 depicts the applied boundary conditions. For clarity, the arrows indicating the cross-wise link conditions for $\bar{u}^\times_z$ have been neglected in this representation.

6.3 Periodic boundary conditions

At last, a set of periodic boundary conditions (pbc) is introduced. Now, the in-plane and out-of-plane displacements $\bar{u}^\parallel_x$ and $\bar{u}^\parallel_y$ are linked symmetrically for each lateral surface. Again, the vertical displacement $\bar{u}^\times_z$ is linked in an anti-symmetric way to avoid rigid body rotations. Table 2 summarizes the boundary and linking conditions. Here, the shear strains are applied to the RVE by means of the presented transition element, refer to Sect. 5.3. It is applied to two vertical faces of the RVE at $x = l_x/2$ and $y = l_y/2$, see dashed lines in Fig. 11. Using the rotational node the shear strains can be applied implicitly on the RVE. In contrast to the traction boundary conditions, the displacement node $\mathbf{u}_{S0}$ of the transition element is not needed. Both matrices from Eq. 75 have to be defined. For the geometric part, the relation between macroscopic and mesoscopic values reads

$$\begin{bmatrix} \bar{u}_x \\ \bar{u}_y \end{bmatrix}_J = \underbrace{\begin{bmatrix} \Delta x & 0 & \frac{1}{2}\Delta y & \Delta x\,z & 0 & \frac{1}{2}\Delta y\,z & 0 & 0 \\ 0 & \Delta y & \frac{1}{2}\Delta x & 0 & \Delta y\,z & \frac{1}{2}\Delta x\,z & 0 & 0 \end{bmatrix}}_{\tilde{\mathbf{A}}^{pbc}_J} \boldsymbol{\varepsilon}^M. \tag{80}$$

For the transition element, only the rotations are prescribed via

$$\begin{bmatrix} \bar{\omega}_x \\ \bar{\omega}_y \end{bmatrix}_I = \underbrace{\begin{bmatrix} 0 & 0 & 0 & 0 & -y & -\frac{1}{2}x & 0 & -1 \\ 0 & 0 & 0 & x & 0 & \frac{1}{2}y & 1 & 0 \end{bmatrix}}_{\hat{\mathbf{A}}^{pbc}_I} \boldsymbol{\varepsilon}^M \tag{81}$$

The control point displacements $\mathbf{u}_J$ are prescribed using the size of the RVE, which corresponds to the coordinate difference of the linked control points $\Delta\mathbf{X} = \mathbf{X}^+ - \mathbf{X}^-$.

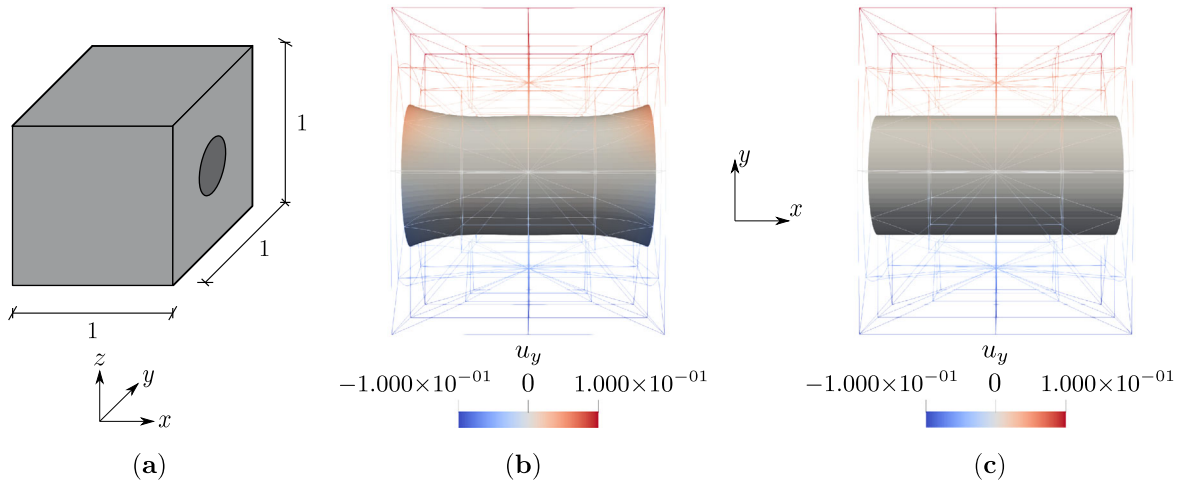

Fig. 9 **a** Perspective view of an RVE with circular inclusion and the plane view of the deformed configuration when ε^M_{yy} is applied for **b** the boundary conditions presented in [21] and **c** the proposed shell boundary conditions

Table 1 Boundary conditions and link conditions for shell type boundary conditions (sbc)

Control points J on	Boundary conditions	Link conditions
Face: $x = \pm l_x/2$	$\bar{\mathbf{u}}_J = \mathbf{A}_J^{sbc}(x, y, z)\,\boldsymbol{\varepsilon}^M$	$u_y(l_x/2, y, z) = u_y(-l_x/2, y, z)$
		$u_z(l_x/2, y, z) = u_z(-l_x/2, -y, z)$
Face: $y = \pm l_y/2$	$\bar{\mathbf{u}}_J = \mathbf{A}_J^{sbc}(x, y, z)\,\boldsymbol{\varepsilon}^M$	$u_x(x, l_y/2, z) = u_x(x, -l_y/2, z)$
		$u_z(x, l_y/2, z) = u_z(-x, -l_y/2, z)$

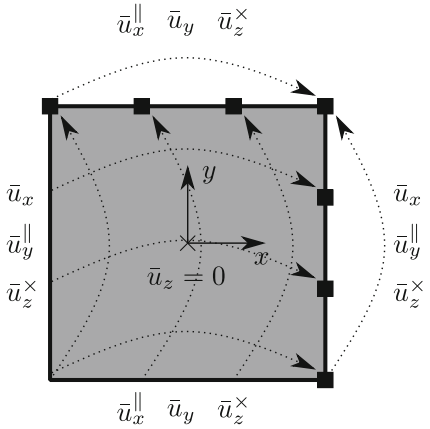

Fig. 10 Plane view of RVE-sbc: Displacements in the out-of-plane direction prescribed, displacements in in-plane and vertical direction linked

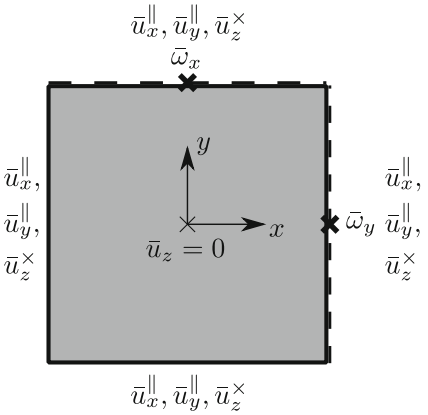

Fig. 11 Plane view of RVE-pbc: all displacements linked, in-plane rotation prescribed using transition element

6.4 Comparison concerning shear application

One of the main differences between the three boundary conditions is the different application of shear strains to the RVE. For the case of a linear-elastic, homogeneous RVE ($E = 100$ [N/mm^2], $\nu = 0.3$) with dimensions $l_x \times l_y \times h = 1 \times 1 \times 1$ [mm×mm×mm] the analytical shear stress distribution reads

$$\begin{aligned}\tau_{xz}(z) &= \frac{3}{2}\frac{Q}{A}\left(1 - \frac{4z^2}{h^2}\right) \\ &= \frac{3}{2}\kappa\, G\, \gamma_x^M (1 - 4z^2).\end{aligned} \tag{82}$$

For $\gamma_x^M = 0.2$ the maximum shear stress takes the value

$$\tau_{xz,max}(z = 0) = \frac{3}{2}\kappa\, G\, \gamma_x^M = 9.615\ [\mathrm{N/mm^2}]. \tag{83}$$

Here, the shear correction factor for rectangular cross-sections $\kappa = 5/6$ was used. Similarly, the displacement due to shear strain γ_x^M can be derived as

$$u_x = \int_{h^{RVE}} \gamma(z)\mathrm{d}z = \frac{5}{4}\gamma_x^M (z - \frac{4}{3}z^3). \tag{84}$$

The analytical maximum displacement is obtained as

$$u_{x,max}(z = \pm h/2) = \pm 0.08\overline{3}\ [\mathrm{mm}]. \tag{85}$$

For this example, the deformation and shear stress distributions for γ_x^M are presented. However, the same applies for the deformation due to an applied γ_y^M. The scaling centre for the RVE discretisation lies in the centre of mass. A discretisation with $n_c = 2$ and $n_b = 6$ elements and polynomial order $p_c = p_b = 4$ is chosen. Additionally, the boundary conditions differ in their symmetry requirements

Table 2 Boundary conditions and link conditions for periodic boundary conditions (pbc)

Control points J on	Boundary conditions	Link conditions
Face: $x = \pm l_x/2$	$\bar{\mathbf{u}}_J = \tilde{\mathbf{A}}_J^{pbc}(x, y, z)\,\boldsymbol{\varepsilon}^M$	$u_x(l_x/2, y, z) = u_x(-l_x/2, y, z)$
		$u_y(l_x/2, y, z) = u_y(-l_x/2, y, z)$
		$u_z(l_x/2, y, z) = u_z(-l_x/2, -y, z)$
Face: $y = \pm l_y/2$	$\bar{\mathbf{u}}_J = \tilde{\mathbf{A}}_J^{pbc}(x, y, z)\,\boldsymbol{\varepsilon}^M$	$u_x(x, l_y/2, z) = u_x(x, -l_y/2, z)$
		$u_y(x, l_y/2, z) = u_y(x, -l_y/2, z)$
		$u_z(x, l_y/2, z) = u_z(-x, -l_y/2, z)$

on the RVE. Figure 12 compares the symmetry requirements, deformed mesh and shear stress distribution for the three different boundary conditions. Traction, shell and periodic boundary condition correspond the first, second and third column of Fig. 12, respectively. The first row presents a plane view of the RVE with two representative inclusions. These are arranged such that the symmetry requirements of the boundary conditions are fulfilled. The second row shows the deformation of the RVE due to an applied shear strain γ_x^M. In the third row the shear stress distribution over the height of the RVE is plotted. Additionally to the analytical solution from Eq. 82, the shear stress distribution on the surface of the RVE (at $(x, y) = (0.5, 0)$) and inside at $(x, y) = (0.25, 0)$ are shown. In Fig. 12a the plane-view, the shear deformation for γ_x^M and the shear stress distribution over the RVE height are depicted for the introduced traction boundary conditions (tbc). Since the shell strains are applied only by means of the transition elements on each lateral surface, there are no symmetry requirements for the RVE. Thus, the inclusions may be distributed randomly in the RVE. Furthermore, using the transition element enforces the deformation in an averaged sense using Langrange multipliers. Thus, cross-sectional warping is possible, which can be seen in the deformed mode. Furthermore, the analytical maximum displacement u_x from Eq. 85 is well approximated. Looking at the shear stress distribution it becomes obvious why the term *traction boundary conditions* is justified. On the surface of the RVE, at $(x, y) = (0.5, 0)$, an almost constant shear stress distribution is obtained. Closer to the centre of the RVE the expected shear stress parabola is closely approximated. Furthermore, the shear stress at the top and bottom surface of the RVE tends to zero which shows, that the zero-traction boundary condition is fulfilled.

In Fig. 12b a plane view, the shear deformation and shear stress distribution are plotted for the shell boundary conditions. Because the in-plane displacements are linked symmetrically and the displacements in the thickness direction are linked in an anti-symmetric way, the mesostructure must be symmetrical and point symmetrical, as indicated by the plane view in Fig. 12. By prescribing the out-of-plane displacement no warping of the cross-section is admissible. Therefore, a linear displacement distribution of the cross-section is obtained. The maximum displacement value corresponds directly to the linear relationship between displacement and shear strain which has been stated in Eq. 27. The shear stress distribution at the surface and inside the RVE approximates a parabola, however, the maximum value is too low, compare Eq. 83. Furthermore, on the surface of the RVE boundary effects at the top and bottom surface can be observed. However, towards the centre of the RVE the approximation of the shear stress parabola becomes better and the shear stress at $z = \pm h/2$ reduces to zero, which shows that the zero-traction boundary condition are fulfilled for the shell boundary conditions.

For the periodic boundary conditions a plane view, the deformation figure and shear stress distribution are depicted for the homogeneous linear-elastic RVE, see Fig. 12c. Due to the linking conditions, again, symmetry and point symmetry is required. The correct maximum displacement from Eq. 85 is obtained and the boundary conditions allow warping of the cross-section. The shear stress distribution, both on the boundary and inside the RVE, takes the expected parabolic shape and the maximum shear stress from Eq. 83 is obtained. The current section has been restricted to consideration of the shear strains, since this is where the most significant differences between the boundary conditions occur. Nevertheless, the deformation figures for the remaining shell strains are exemplarily shown in Appendix A for all three types of boundary conditions. It can be seen that the deformation modes are correctly represented regardless of the boundary conditions.

7 Numerical examples

The developed multiscale approach is implemented in an extended version of the academic finite element analysis program FEAP [37]. First, the approach is verified on the mesoscale comparing the numerical solutions with analytical values. The three different kinds of boundary conditions presented in Sect. 6 are compared to each other. Furthermore, coupled multiscale problems are investigated. Comparisons are made with analytical and full-scale solutions.

7.1 Verification on the mesoscale

The stiffness of the Reissner–Mindlin shell theory was introduced in Sect. 2 as the shell material tangent $\mathbb{D}$. The components for the linear-elastic, isotropic case were specified in Eq. 26. The analytical stiffness components are used as a reference to verify the numerical method. In a first step, homogeneous and layered RVEs with linear-elastic, isotropic material are considered, because for these the analytical solutions can be derived. Generally, the scaled boundary isogeometric analysis is used for solution of the mesoscopic boundary value problem. Unless otherwise stated converged stiffness values are used for comparison. For simplicity the sections are discretised conforming and using the same polynomial degree and number of elements in boundary and scaling direction. Thus, $p_c = p_b$ and $n_c = n_b$ applies. As a starting point $p_c = p_b = 3$ and $n_c = n_b = 2, 4, 6, 8$ is chosen. However, a full convergence study on the mesoscale is out of the scope of the present work. For simplicity the scaling

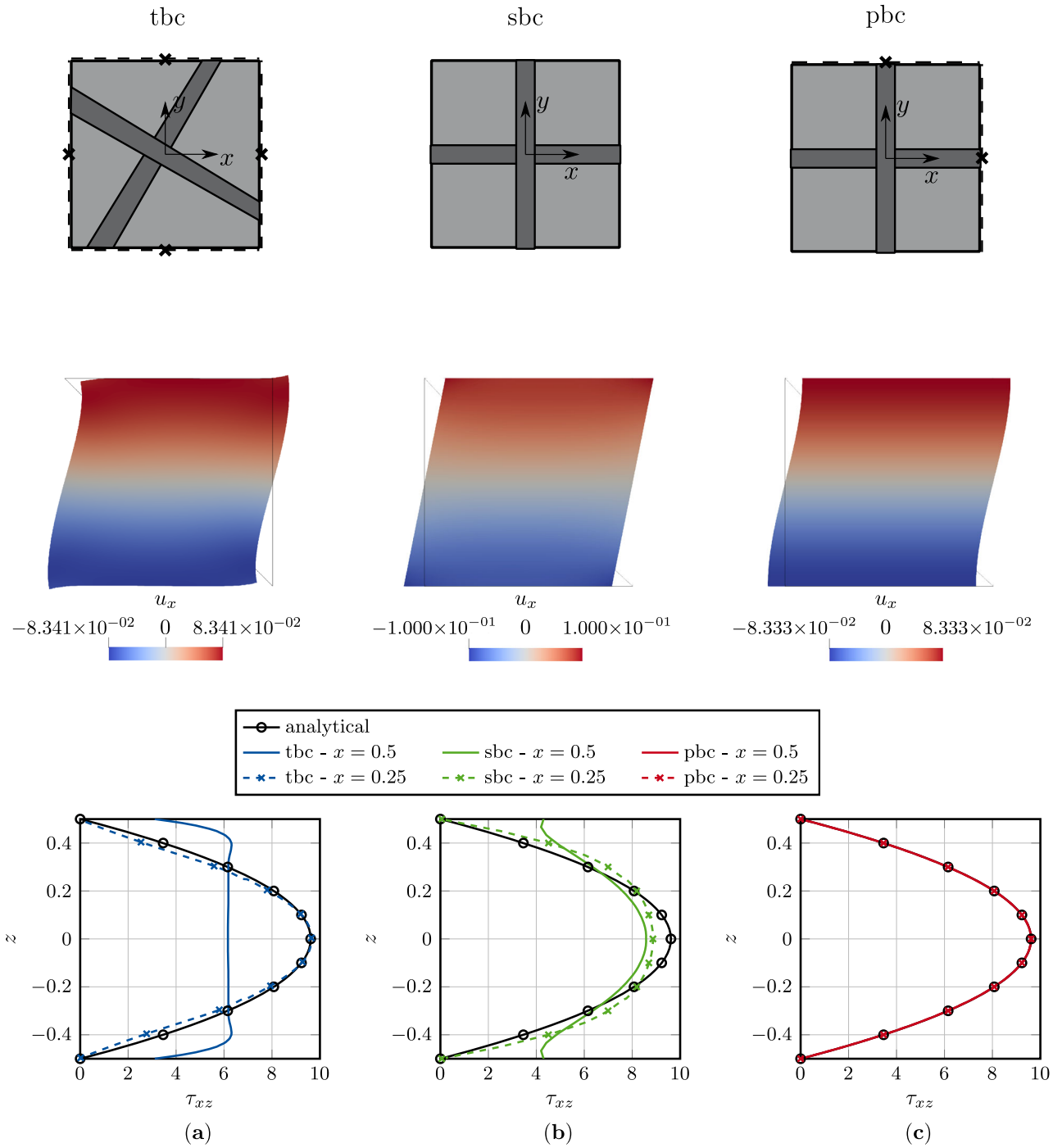

Fig. 12 Comparison of symmetry requirements, shear deformation and shear stress distribution for $\gamma_x = 0.2$ for **a** traction boundary conditions, **b** shell boundary conditions and **c** periodic boundary conditions

center C is chosen to lie in the centre of mass of each section. In the following the robustness of the presented approaches with respect to the length scale of the RVE is examined. The respective length L^{RVE} is increased by repetition of a single RVE in both in-plane directions. The stiffness components are compared for the three different types of boundary conditions.

7.1.1 Homogeneous linear elastic RVE

To begin with, a RVE of dimensions $1\times1\times1$ [mm×mm×mm] is considered, as depicted in Fig. 13. A linear elastic isotropic material with Young's Modulus $E = 100$ [N/mm^2] and Poisson's ratio $\nu = 0.3$ is assumed. To investigate the influence of the length scale of the RVE, the dimensions of

$L^{RVE} = l_x = l_y$ are consecutively increased, while the height is kept constant.

The numerical solution evaluating Eq. 73 yields the zero entries in Eq. 24. The results for the non-zero entries are summarised in Table 3 for different the boundary conditions. The traction boundary conditions exhibit a length dependency for the torsional stiffness D_b^{33} and the shear stiffnesses $\mathbb{D}_s$. For the homogeneous case $D_s^{11} = D_s^{22}$ holds. The shell boundary conditions show a length dependent behaviour for the shear stiffnesses while the periodic boundary conditions directly yield the analytical values for all components. Figure 14 shows the relation of the obtained numerical stiffness to the calculated analytical stiffness $D_{num}/D_{analytical}$ for different RVE lengths. Figure 14a illustrates the length dependency of the torsional stiffness D_b^{33} for the traction boundary conditions. In Fig. 14b the numerical solution for the shear stiffness $D_{s,num} = G\, h_s$ is compared to the analytical value $D_{s,analytical} = G\, h$ resulting in the numerical shear correction factor κ. For the rectangular cross-section the analytical value is $\kappa_{ref} = 5/6$, which is obtained using periodic boundary conditions irrespective of L^{RVE}.

For all three boundary conditions the introduced moment reduction constraint from Sect. 5.4 is employed. To show the necessity of the constraint the same example has been investigated without it. The results are presented in "Appendix B".

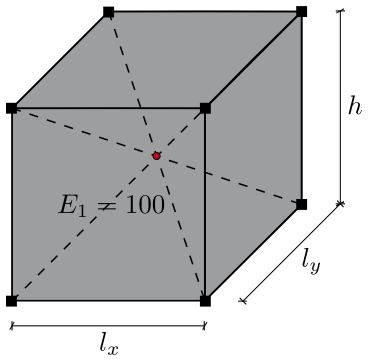

Fig. 13 Exemplary homogeneous RVE of dimensions $1 \times 1 \times 1$

7.1.2 Layered linear elastic RVE

In a next step a layered mesostructure is considered. The height is kept constant as $h = 1$ [mm] and the three layers take equal thickness of $h_l = \frac{1}{3}$ [mm], compare Fig. 15. Again, linear elastic material behaviour is assumed where the face sheets have a Young's modulus $E_1 = 100$ [N/mm^2] and the core is 10 times stiffer with $E_2 = 1000$ [N/mm^2]. The Poisson's ratio for both materials is $\nu = 0.3$. Using Eq. 24 the analytical stiffness components for layered microstructures can be calculated. The shear correction factor is determined as $\kappa_{ref} = 0.625$, according to [39]. The non-zero stiffness components from Eq. 24 for the different boundary conditions are summarised in Table 4. To investigate the length dependency, again the lengths $L^{RVE} = l_x = l_y$ are increased, while $h = 1$ [mm] is kept constant. The results are presented in Fig. 16. Figure 16a illustrates the length dependency of the torsional stiffness D_b^{33} using traction boundary conditions (tbc). In Fig. 16b the shear correction factor is depicted. Again, a length dependency for traction and shell boundary conditions is observed.

7.1.3 Shear correction factor for layered RVE

From the observations on the homogeneous and layered RVE the homogenized stiffness components seem to exhibit no length dependency using the periodic boundary conditions, which is desirable in order to minimise the computational effort. To investigate this further for different layered RVEs the core fraction ρ_C and stiffness ratio α is varied and the shear correction factor κ is obtained numerically using only periodic boundary conditions. An RVE of dimensions $l_x \times l_y \times h = 1 \times 1 \times 1$ [mm $\times$ mm $\times$ mm] is used. The height of the different layers depends on the core fraction ρ_C, which describes the ratio between the height of the core and the total RVE height $h_C = \rho_C h$. Therefore, the thickness of the two face layers is given as $h_L = (h - h_C)/2$ and the total height reads $h = h_C + 2h_L$. The factor α is introduced to relate the core and layer stiffnesses to each other by means of their respective Young's moduli using $E_C = \alpha E_L$. An analytical solution for the shear correction factor of layered cross-sections can be found in [39] and is calculated as

Table 3 Comparison of stiffness components for different boundary conditions—homogeneous RVE

Stiffness component	Traction b.c. (tbc)	Shell b.c. (sbc)	Periodic b.c. (pbc)
$\mathbb{D}_m$	Exact	Exact	Exact
$\mathbb{D}_{mb}$	Exact	Exact	Exact
$D_b^{11}, D_b^{22}, D_b^{12}$	Exact	Exact	Exact
D_b^{33}	See Fig. 14a	Exact	Exact
$\mathbb{D}_s$	See Fig. 14b	See Fig. 14b	Exact

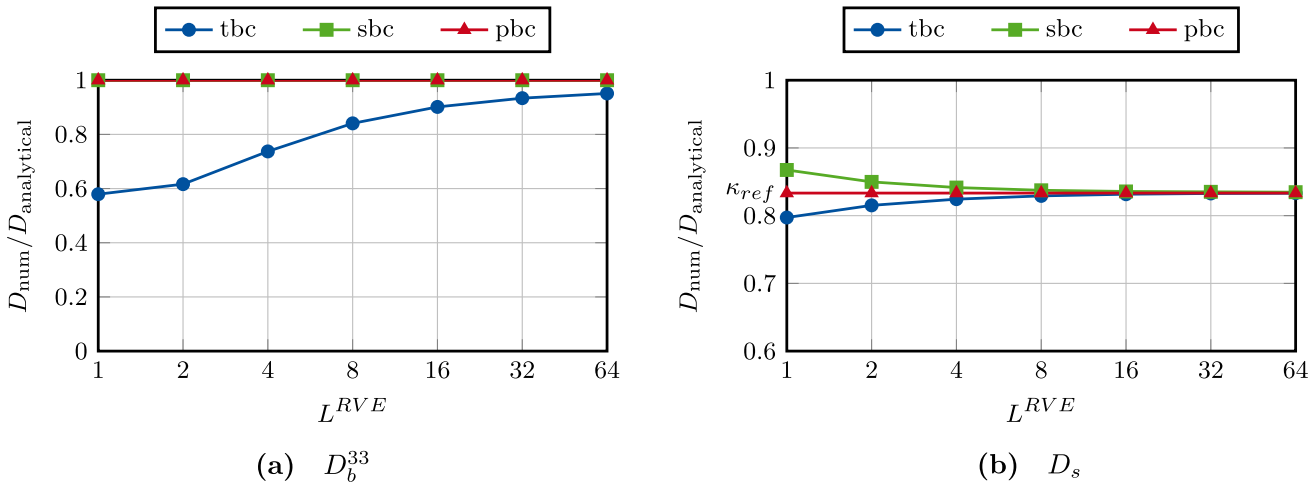

(a) D_b^{33} (b) D_s

Fig. 14 Length dependency of the stiffness components D_b^{33} and $D_s^{11} = D_s^{22}$ for different boundary conditions for a homogeneous RVE

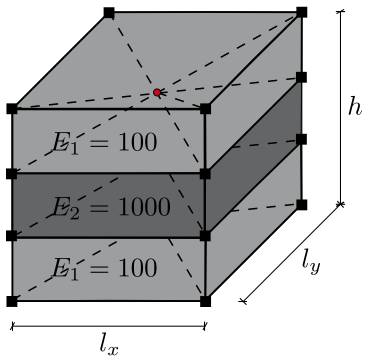

Fig. 15 Exemplary layered RVE of dimensions $1 \times 1 \times 1$

$$\kappa = \frac{4}{9}\frac{T_1^2}{T_2 T_4}. \tag{86}$$

The components T_1, T_2 and T_4 are calculated as follows

$$T_1(\rho_C) = (1-\rho_C^3) + \rho_C^3\alpha$$
$$T_2(\rho_C) = \frac{(1-\rho_C)}{\alpha} + \rho_C$$
$$T_3(\rho_C) = (1-\rho_C^2)^2 + \frac{8}{15}\alpha^2\rho_C^4 + \frac{4}{3}\alpha\rho_C^2(1-\rho_C^2)$$
$$T_4(\rho_C) = A(\rho_C)\alpha + \rho_C T_3$$
$$A(\rho_C) = \frac{(1-\rho_C)^3}{15}(3\rho_C^2 + 9\rho_C + 8). \tag{87}$$

The results for $\rho_C = 0.2, 0.4, 0.6, 0.8$ and $\alpha = 0.1, 0.5, 10$ are given in Fig. 18. The analytical solution are represented with continuous lines and the numerical results are depicted with symbols. For all stiffness ratios α and core fractions ρ_C very good agreement between the numerical and analytical solution is obtained. For $\rho_C = 0$ and $\rho_C = 1$ the cross-section is homogeneous, which has already been examined in Sect. 7.1.1. Additionally, the values obtained by the authors of [23] for $\alpha = 0.1$ and different core fractions are depicted. For comparison, the boundary conditions are employed neglecting the stiffness jumps over the cross-section height. Because the moment reduction constraint assumes a homogeneous material, in this case, it is abbreviated as 'hMRC'. The results are shown in Fig. 18, indicated by crosses. Good agreement between the results from [23] and the proposed periodic boundary conditions neglecting the stiffness jumps can be observed, which indicates that the introduced moment reduction constraint is comparable to the constraint on the fluctuation moment introduced by [23]. By incorporating the stiffness jumps across the thickness h of the RVE, the obtained shear correction factors lie closer to the analytical solution. The analytical

Table 4 Comparison of stiffness components for different boundary conditions—layered RVE

Stiffness component	Traction b.c. (tbc)	Shell b.c. (sbc)	Periodic b.c. (pbc)
$\mathbb{D}_m$	Exact	Exact	Exact
$\mathbb{D}_{mb}$	Exact	Exact	Exact
D_b^{11},D_b^{22},D_b^{12}	Exact	Exact	Exact
D_b^{33}	see Fig. 16a	Exact	Exact
$\mathbb{D}_s$	See Fig. 16b	See Fig. 16b	Exact

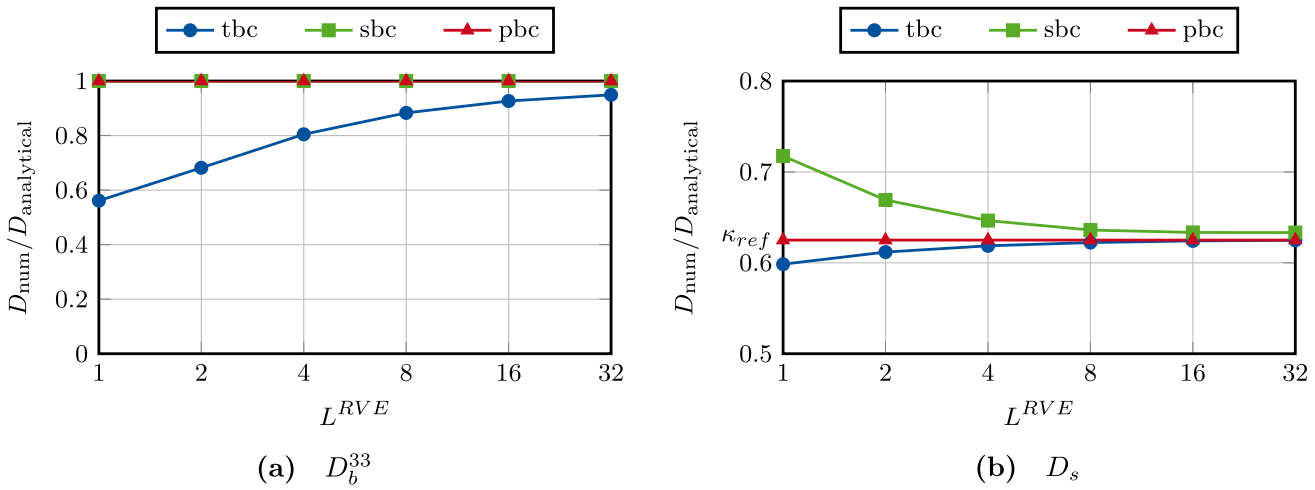

Fig. 16 Length dependency of the stiffness components D_b^{33} and $D_s^{11} = D_s^{22}$ for different boundary conditions for a layered RVE

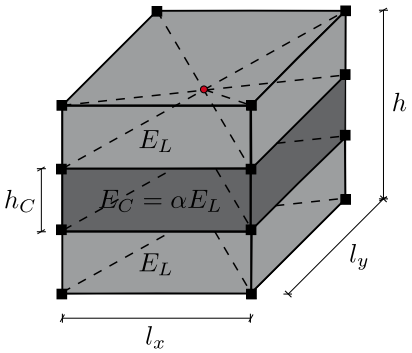

Fig. 17 Dimensions of a RVE with different core fraction ρ_C and stiffness ratio α

shear correction factors, as well as the ones obtained by periodic boundary conditions with and without considering stiffness jumps are summarized in Table 5. Considering the stiffness jumps the error between numerical and analytical solution is neglectable. However, assuming homogeneous cross-sections for the moment reduction constraint the error becomes noticeable.

Thus, the presented periodic boundary conditions are able to correctly calculate all stiffness components $\mathbb{D}$ for homogeneous and layered RVEs irrespective of L^{RVE}.

7.2 Verification on the macroscale

Four different coupled problems are investigated. On the macroscale a 5/6-parameter 4-node shell element is used. Reference solutions are obtained either analytically or by full-scale models. Displacement-based volume elements with quadratic Lagrange shape functions are used for comparison. If not stated otherwise the same general concepts for the discretisation and the position of the scaling center on the mesoscale apply. It is important to note, that the thickness of the shell always coincides with the height of the RVE, therefore $h^M = h^{RVE} = h$. For the examples with linear-elastic material behaviour the macroscopic material parameters were obtained by homogenization of a single RVE.

7.2.1 Beam

As a first example, a clamped beam of length $L = 6,\ 20$ [cm], height $h = 1$ [cm] and width $B = 1$ [cm] is examined, compare Fig. 19. It is loaded by a distributed load $p = 1$ [N/cm]. The clamping is free of constraint forces. Two different beam lengths, $L = 6$ [cm] and $L = 20$ [cm], are examined, because for the long beam the influence of the shear stiffness is significantly lower than for the shorter beam. Three different kinds of mesostructures are considered. Initially, a homogeneous mesostructure (Fig. 19a) is considered, in order to investigate the length dependency of the stiffness components on the RVE size and the influence of the beam length L. Next, the cross-section is reinforced, using a circular inclusion with radius $r = 1.06$ [mm], in length direction of the beam (Fig. 19b) and perpendicular to the same (Fig. 19c). Figure 19 shows one representative volume element of dimensions $l_x = l_y = h = 1$ [cm], which is also referred to as unit cell, for each configuration. The macroscopic full-scale volume model is composed of several RVEs positioned next to each other. Thus, if the fibre is oriented parallel to the y-axis, the distance between their centre axes is equal to $B = 1$ [cm].

The vertical tip displacement u_z in point A of the beam is compared. For this example the reinforcement is chosen to lie within the centre line of the beam, which is physically meaningless. However, it is considered sufficient since the

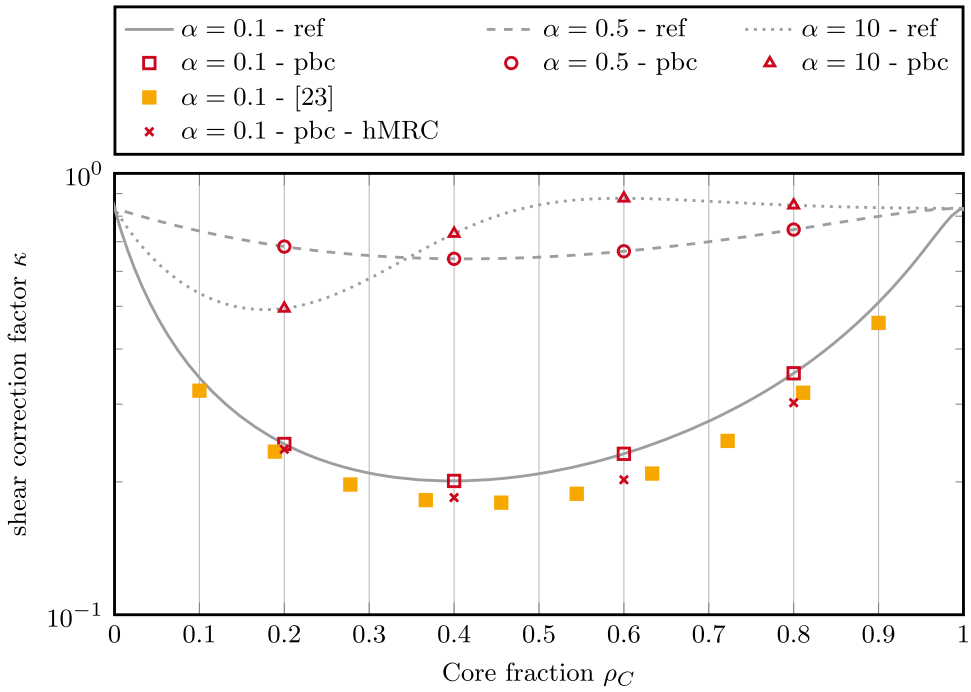

Fig. 18 Shear correction factor κ for different core fractions ρ_C and stiffness ratios α

Table 5 Comparison of shear correction factors κ for $\alpha = 0.1$ and different core fractions ρ_C

ρ_c	κ			$\|\|(\kappa - \kappa_{ref})/\kappa_{ref}\|\|$	
	ref	pbc	pbc-hMRC	pbc	pbc-hMRC
0.2	0.2437108	0.2437108	0.2371071	7.3261×10^{-8}	2.7096×10^{-2}
0.4	0.2009883	0.2009884	0.1843120	9.7180×10^{-8}	8.2971×10^{-2}
0.6	0.2315657	0.2315656	0.2022446	2.0274×10^{-7}	1.2662×10^{-1}
0.8	0.3525041	0.3525041	0.3022766	3.1180×10^{-8}	1.4249×10^{-1}

focus is on the different orientation and its implication on the chosen boundary conditions.

Homogeneous Initially, homogeneous material is assumed to investigate the influence of the length of the beam L and the influence of the type of boundary condition. Linear-elastic material behaviour with Young's modulus $E = 100$ [N/cm^2]

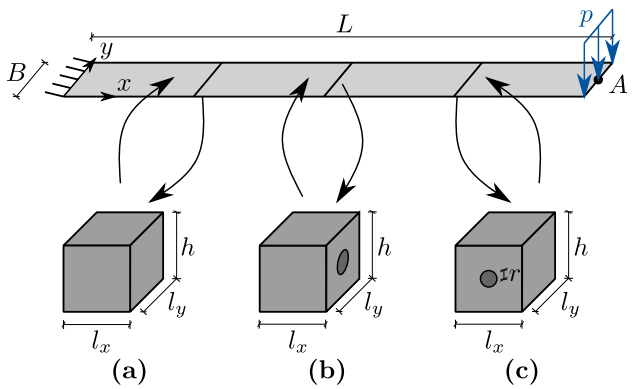

Fig. 19 Clamped beam subjected to load p with three different RVEs—**a** homogeneous **b** reinforcement in length direction **c** reinforcement in width direction

and Poisson's ratio $\nu = 0.3$ is employed. The macroscopic shell is meshed using one element in width direction. In length direction the number of elements is chosen depending on the beam length L. For the presented examples $numel = 32 \cdot L$ is chosen. Thus, for $L = 6$ [cm] $numel$=192×1 and for $L = 20$ [cm] $numel$=640×1. This leads to very fine meshes. However, because the present contribution is concerned with the influence of the RVE length L^{RVE} and the comparison of the three types of boundary conditions, this fine discretisation is chosen to avoid additional effects from macroscopic mesh refinement. On the mesoscale the size of the RVE is chosen as $L^{RVE} = 1, 2, 4, 8$ [cm] to show the effect of length dependency. The error of the numerical result is estimated with respect to the analytical solution, which is obtained from beam kinematics as

$$u_z = u_{z,B} + u_{z,S} = \frac{FL^3}{3EI} + \frac{FL}{GA_s}. \tag{88}$$

Where $F = p \cdot B$ is the resulting load and A_s the cross-sectional shear area of the beam, taking into account the shear correction factor $\kappa = 5/6$.

The results for the short beam with $L = 6$ [cm] are depicted in Fig. 20a. The relative error is plotted versus the size of the RVE for the three different boundary conditions. The results are in line with the observations made in Sect. 7.1. While for traction and shell boundary conditions a length dependency is observed, the periodic boundary conditions show good agreement with the analytical solution independent of the RVE size.

Similar observations are made for a long beam with $L = 20$ [cm], see Fig. 20b. Note, that the error is a factor ten smaller than for the short beam. This is due to the fact, that the (length dependent) shear stiffness influences the overall displacement stronger for smaller length to height ratios.

Longitudinal reinforcement The beam is now reinforced with one longitudinal fibre in length direction of the beam, as depicted in Fig. 19b. The fibre is assumed to be circular with a radius of $r = 1.06$ [mm]. Width and height of the RVE are initially assumed to be $l_x = l_y = h = 1$ [cm]. For matrix and fibre a linear-elastic material behaviour is assumed, where the fibre is approximately five times stiffer than the matrix. The material parameters are based on typical values for concrete and carbon-textile reinforcement and can be found in Table 6. The macroscopic shell is again discretised using $32 \cdot L \times 1$ ($L \times B$) elements, which leads to a converged solution. On the mesoscale the size of the RVE is chosen as $L^{RVE} = 1, 2, 4$ to show the effect of length dependent stiffness components. For $L^{RVE} = 1$ the RVE corresponds to the unit cell, for $L^{RVE} > 1$ the RVE consists of multiple unit cells positioned next to each other. As before, the maximum vertical tip displacement u_z in point A is observed. As there is no analytical solution for this case available, a full-scale solution has been calculated using a standard quadrilateral element with quadratic shape functions. In order to obtain the same boundary conditions with the volume solution as with the shell solution, three types of boundary conditions are applied. Figure 21 schematically depicts the boundary conditions. For all cases the length direction (x-axis) of the beam is fully fixed, whereas the out-of-plane direction (y-axis) is fixed in only one point of the beam to allow for transverse deformation. The three options differ in the boundary conditions for the thickness direction (z-axis). For option (i), see Fig. 21a, the whole beam is fixed in thickness direction which yields a lower bound solution. For case (iii) only the centre axis is fixed in thicknes direction, compare Fig. 21c. This leads to an upper bound for the displacement. Because fixing the thickness direction in the centre axis in (iii) introduces a singularity, for (ii) the load p is applied additionally in opposite direction at the fixed edge. This enforces a global equilibrium in thickness direction, reduces the singularity and gives an intermediate reference solution, compare Fig. 21b. The beam is discretised using 38,160 and 126,864 elements for $L = 6$ [cm] and $L = 20$ [cm], respectively. For the circumferential direction of the fibre 16 elements are used. For comparison the average of the maximum and minimum displacement over the height is used.

Table 6 Material parameters for the fibre-reinforced beam

	Matrix	Fibre
E [N/mm^2]	27000	142000
ν [–]	0.2	0.35

The results are given in Fig. 22. Absolute displacements u_z of the converged mesh are compared for different RVE sizes, different boundary conditions and the two beam lengths L. In Fig. 22a the displacement u_z for different RVE sizes and $L = 6$ [cm] is shown. It can be observed, that all solutions lie between the upper and lower bound obtained from the full-scale model. The two reference solutions differ by 0.388%. The traction and displacement boundary condition exhibit a

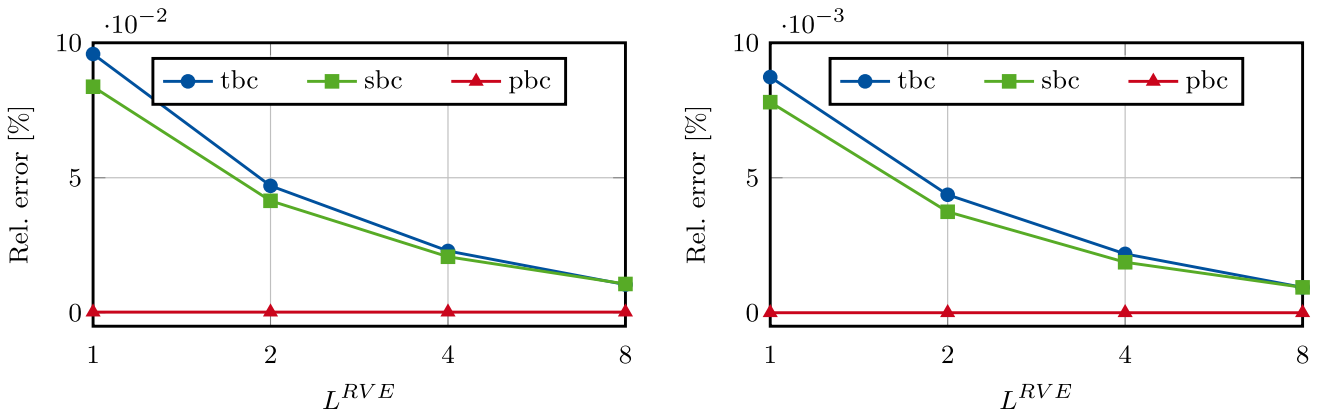

(a) $L = 6$ [cm] **(b)** $L = 20$ [cm]

Fig. 20 Relative error of the vertical tip displacement for different RVE sizes L_{RVE} and different boundary conditions

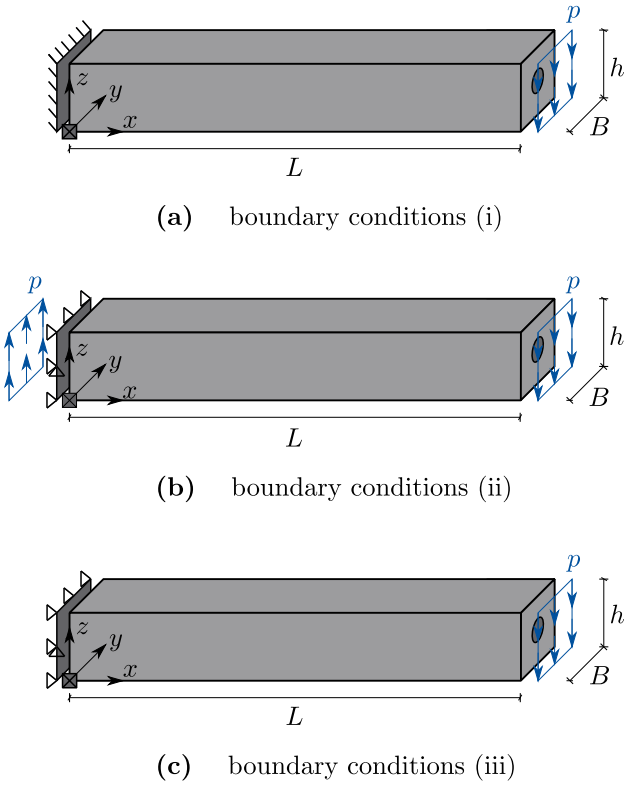

Fig. 21 Full-scale volume model of the longitudinal reinforced beam with different boundary conditions

length dependency, which is again due to the length dependent shear contribution. The periodic boundary conditions yield constant results for different RVE sizes.

For the long beam with $L = 20$, the results are visualized in Fig. 22b. Here the two reference solutions differ only by 0.067%, because boundary effects at the supports are reduced over the length of the beam. Again, all solutions lie within the bounds or in close proximity. Similar as for the homogeneous example, the length dependency of the traction and displacement boundary condition is smaller, due to the reduced shear contribution.

Transverse reinforcement As a last example the beam is now reinforced transversally, see Fig. 19c, to investigate the influence of the fibre direction on the overall behaviour. The dimensions of the fibre and RVE are chosen as before. The same linear-elastic material parameters from Table 6 are used. The macroscopic and mesoscopic meshes remain unchanged. Similarly, an upper and lower bound reference solution is calculated using 38,160 and 126,864 elements for $L = 6$ [cm] and $L = 20$ [cm], respectively. In Fig. 23 the vertical displacement u_z is plotted for the three different boundary conditions and different RVE sizes. Again, all solutions lie well in between the upper and lower bound solution. In contrast to the longitudinal reinforcement a slight length dependent behaviour for the periodic boundary conditions can be observed. Especially for the short beam with $L = 6$ [cm], see Fig. 23a. This can be related to the second additional constraint which reduces the length dependency of the shear stiffnesses, refer to Sect. 5.4. A linear moment distribution is assumed, see Fig. 5, which is not correct for the case of inclusions in the RVE. As long as the inhomogeneity stretches over the whole width the shear stiffness in the respective direction is calculated correctly, e.g. longitudinal reinforcement. The assumption is not sufficient when the inclusion does not stretch over the whole width. However, the length dependency is rather small and is considered neglectable. It should be kept in mind that for larger inclusions and greater stiffness differences between matrix and fibre the assumption of a linear moment distribution might not be adequate.

7.2.2 Layered cylindrical shell

A quarter of a three-layered cylindrical shell is examined, see Fig. 24. For comparison the same geometrical and material properties as in [21] are used. The length $L = 300$ [mm], the radius $R = 100$ [mm] and the thickness is given by $h = 1$ [mm]. For the layers transversal isotropic material behaviour is assumed, the material parameters are given as

$$\begin{aligned} E_1 &= 125000\ \text{N/mm}^2 \quad & G_{12} &= 4800\ \text{N/mm}^2 \\ E_2 &= 7400\ \text{N/mm}^2 \quad & G_{23} &= 2700\ \text{N/mm}^2 \\ \nu_{12} &= 0.34. \end{aligned} \tag{89}$$

The rotation angle of the layers is [90°/0°/90°], where 0° describes the circumferential direction and 90° corresponds to the length direction. The shell is discretised using 16 elements in each direction. For the multiscale approach each layer of the RVE is modelled using $p_c = p_b = 4$ and $n_c = n_b = 2$. As reference the shell element from [40] is used with four elements for each layer. Geometrical nonlinearity is assumed for the macroscopic shell. The displacement u_z is prescribed and the point load F is obtained as reaction force. The load–displacement curve is depicted in Fig. 25. Additionally, the results from [21] are given. It can be seen that the shell formulation as well as the multiscale approach using periodic and shell boundary conditions are in good agreement with the results from [21]. Using small RVEs of dimensions $1 \times 1 \times 1$ [mm×mm×mm] yields sufficient results. For the traction boundary conditions and a RVE of dimension $1 \times 1 \times 1$ [mm×mm×mm] the obtained response is too soft. Increasing L^{RVE} consecutively increases the accuracy of the solution. The length dependency of the traction boundary conditions originate from the torsional stiffnesses D_b^{33}, compare Fig. 16a. The length dependency in shear stiffnesses do not influence the macroscopic behaviour due to the small length to height ratio of the shell.

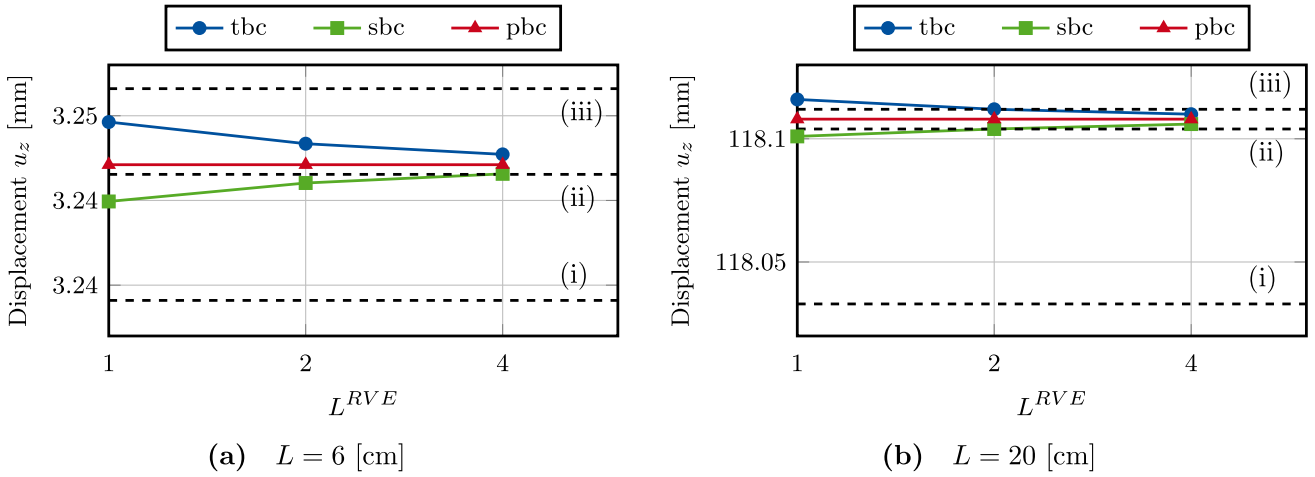

Fig. 22 Comparison of vertical tip displacement for different boundary conditions for longitudinal reinforcement of the beam

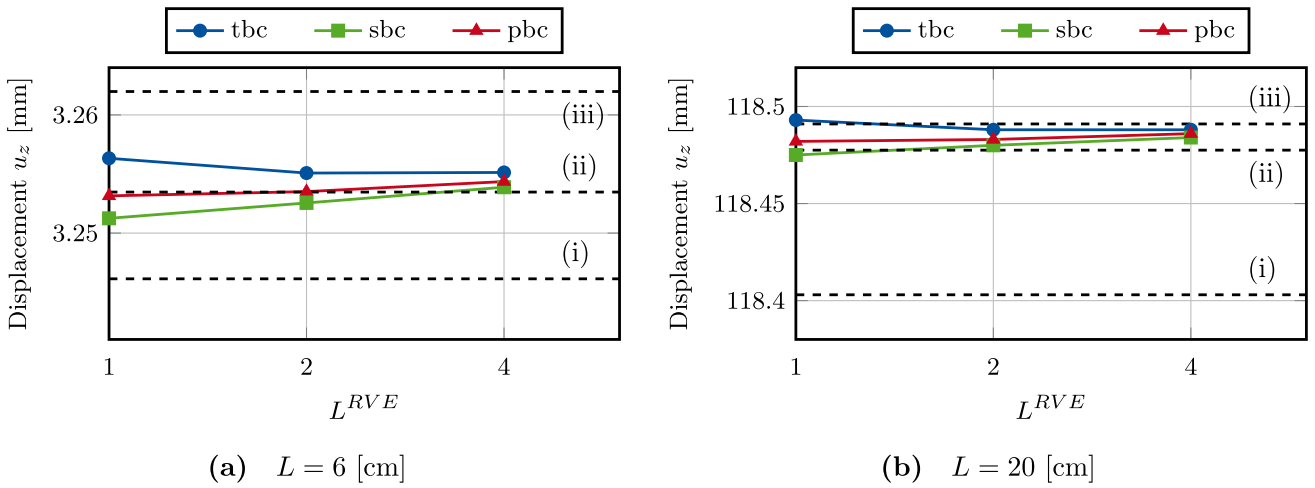

Fig. 23 Comparison of vertical tip displacement for different boundary conditions for transversal reinforcement of the beam

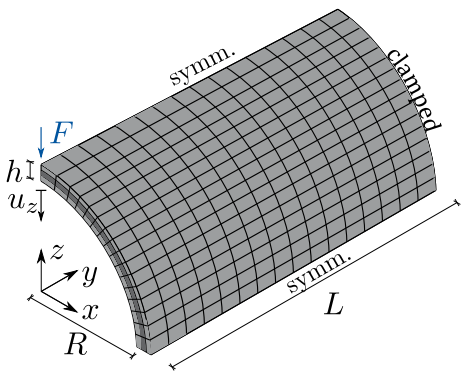

Fig. 24 Quarter of a cylindrical layered shell

7.2.3 Plate: elasto-plastic material

A plate of dimensions B = L = 100 [cm] and thickness h = 1 [cm] is loaded by a uniformly distributed load $p = 0.01$ [kN/cm^2]. Exploiting the symmetry of the plate only one quarter is modelled. The boundary conditions are given in Fig. 26. A small strain elasto-plastic isotropic material law with $E = 210000$ [kN/cm^2], $\nu = 0$ and yield stress $f_{y,k} = 240$ [kN/cm^2] is assumed. For comparison the yield line theory (YLT), which is explained in [41], is used. The plastic moment of the yield line is determined as

$$m_{pl} = \frac{1}{4} h^2 f_{y,k} = 60 \frac{kNm}{m}. \tag{90}$$

For a simply supported plate the ultimate load p can be derived using the principle of virtual displacements, see [41]. Thus, the ultimate load factor λ is written as

$$\lambda\, p = 24 \frac{m_{pl}}{L^2} = 0.144 \frac{kN}{cm^2}, \quad \text{thus} \quad \lambda = 14.4. \tag{91}$$

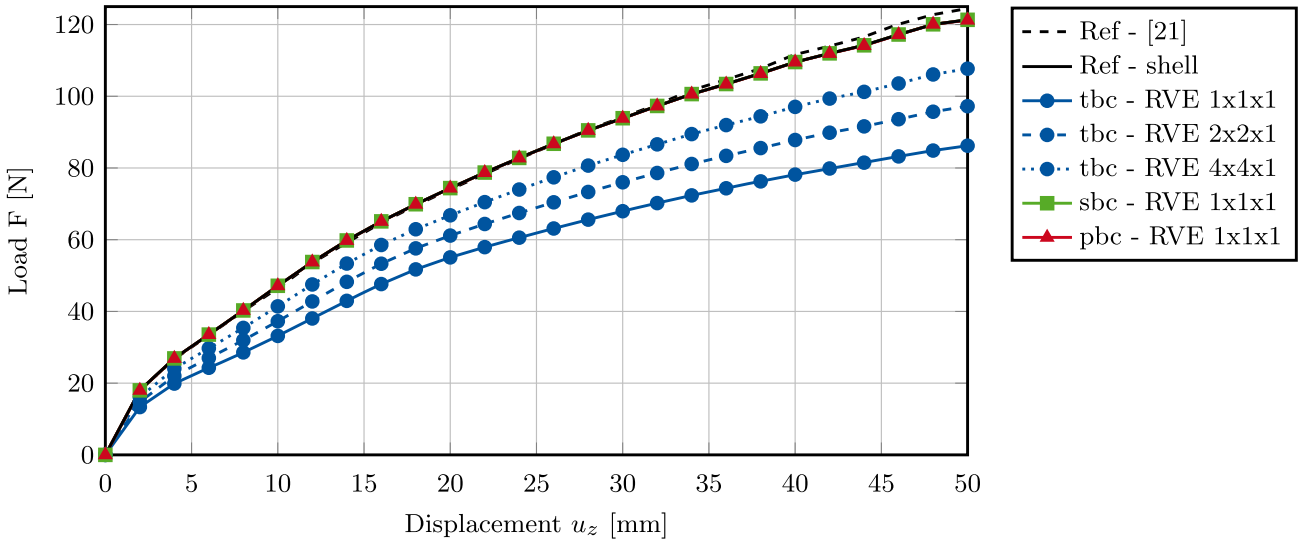

Fig. 25 Load–Displacement curve for the layered cylindrical shell

Furthermore, the shell element from [40] is used with a discretisation of 32×32 elements to model the quarter plate. In thickness direction seven layers are used. For the multiscale approach the size of the RVE is chosen as $L^{RVE} = h = 1$ [cm] and is discretised using polynomial order $p_c = p_b = 3$ and $n_c = n_b = 2$ elements per direction. The macroscopic scale is discretised using 4×4 shell elements. Figure 27 plots the load factor λ against the displacement u_z in point A, compare Fig. 26. The multiscale approach using periodic and shell boundary conditions show good agreement with the shell formulation used as reference. Furthermore, the analytical load factor from yield line theory is closely approximated. As in the previous example, the traction boundary condition for RVEs of size $1 \times 1 \times 1$ [cm×cm×cm] underestimate the solution due to the length dependency in the torsional stiffness components D_b^{33}.

In Fig. 28a the displacement u_z of the reference shell is depicted for $\lambda = 14.4$. Figure 28b shows the von Mises stress distribution at mid-surface $z = 0$ and at the boundary layer $z = \pm h/2$ (Fig. 28c). While at the boundary layer the yield stress is reached in most regions, the mid-surface has not reached yield stress yet. However, the region of highest stress corresponds to the expected yield line. In Fig. 29 the displacement figure of the macroscopic shell is depicted, which corresponds to the reference shell, compare Fig. 28a. For the four corner elements the von Mises stress of the RVE corresponding to the first integration point is depicted. A qualitative comparison of the von Mises stresses in the RVEs to the reference shell at mid and top surface (Fig. 29b, c) shows good agreement.

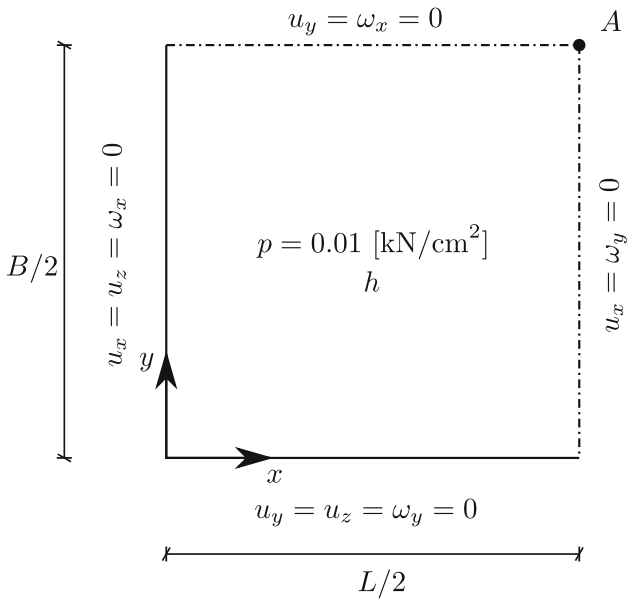

Fig. 26 Geometry and boundary conditions of the plate with elasto-plastic material behaviour

7.2.4 Plate: longitudinally reinforced

A plate of dimensions B = L = 50 [cm] and thickness h = 1 [cm] and longitudinal circular inclusions is loaded by a uniformly distributed load $q = 1$ [N/mm^2]. The radius of the inclusion is again $r = 1.06$ [mm] and the distance between two centre lines is equal to 1 [cm]. Similar to the example in Sect. 7.2.1, for simplicity the reinforcement is positioned vertically centred within the plate. For comparison a full-scale model is inspected. The two configurations are depicted in Fig. 30. To reduce the computational cost the symmetry of the plate is exploited. The boundary conditions for the plate are given in the Table 7. Boundary

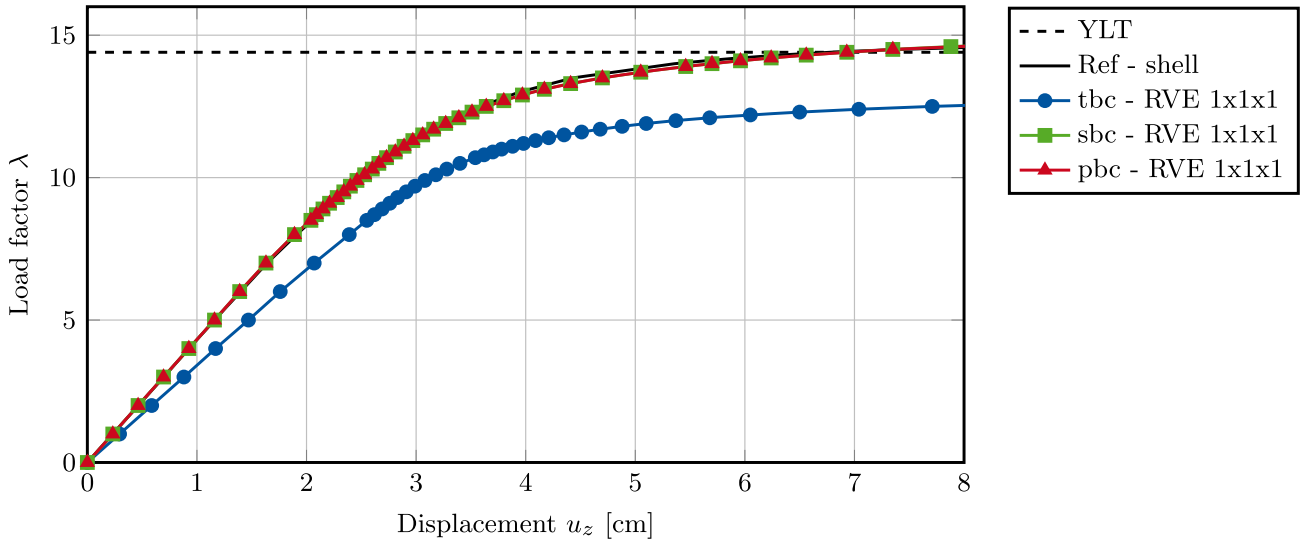

Fig. 27 Load factor λ versus displacement u_z in the centre of the plate

conditions for the full-scale model are applied at $z = 0$, where $-h/2 \leq z \leq h/2$. Linear-elastic material behaviour is used for fibre and matrix, Young's modulus and Poisson's ratio can be taken from Table 6. The vertical displacement u_z at the intersection of the symmetry axes, see Point A in Fig. 30, is determined. For the full-scale solution the displacement is taken as the average of the displacements at $z = h/2$ and $z = 0$. The macroscopic shell is meshed using $numel = 2^2, 4^2, 8^2, 16^2, 32^2, 64^2, 128^2, 256^2, 512^2, 1024^2$ elements. Similar to Sect. 7.2.1 the macroscopic mesh is considerably refined to examine the macroscopic effects of the RVE and reduce the effects from macroscopic mesh refinement.The size of the RVE is varied from $L^{RVE} = 1, 2$ to 4 [cm]. Again, the RVE can comprise multiple unit cells, for example contains a RVE with $L^{RVE} = 4$ [cm] four circular inclusions. The reference solution is obtained using 370,000 quadratic elements. The circular inclusion is approximated using 16 elements in circumferential direction.

In Fig. 31 the vertical displacement u_z is plotted versus the macroscopic number of elements (*numel*) which are used to discretise the shell. In the upper diagram the convergence for all three types of boundary conditions and different RVE sizes is shown. In the lower diagram a section is enlarged which contains the shell and periodic boundary conditions only. It can be seen, that the shell and periodic boundary conditions yield very similar results. Neither approach shows a

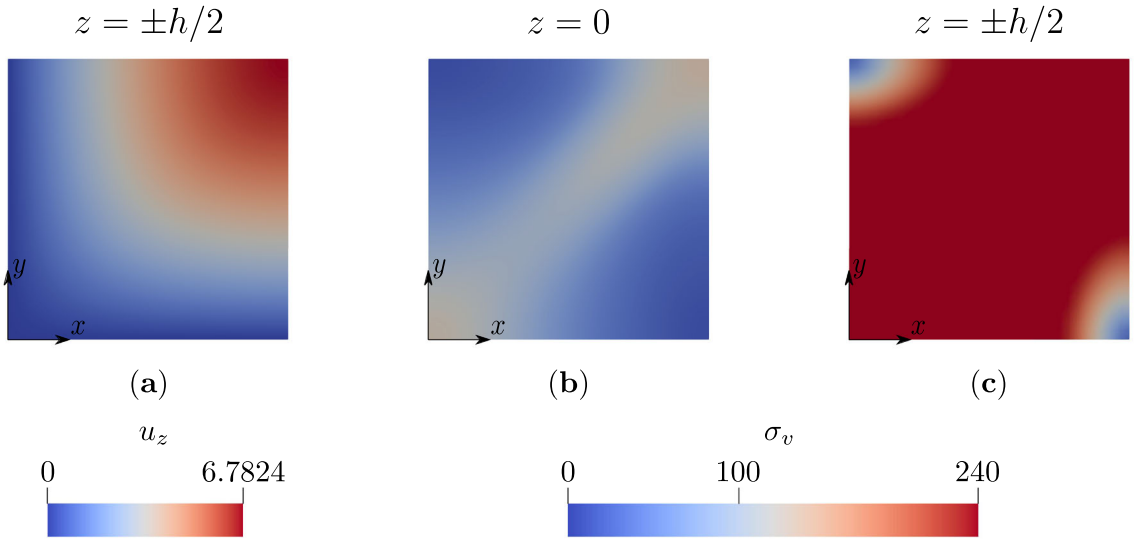

Fig. 28 Contour plot for **a** the displacement u_z [cm] at the boundary layers $z = \pm h/2$ and for the von Mises stress σ_v [kN/cm^2] at **b** mid-surface and **c** top/bottom surface of the reference shell ($\lambda = 14.4$)

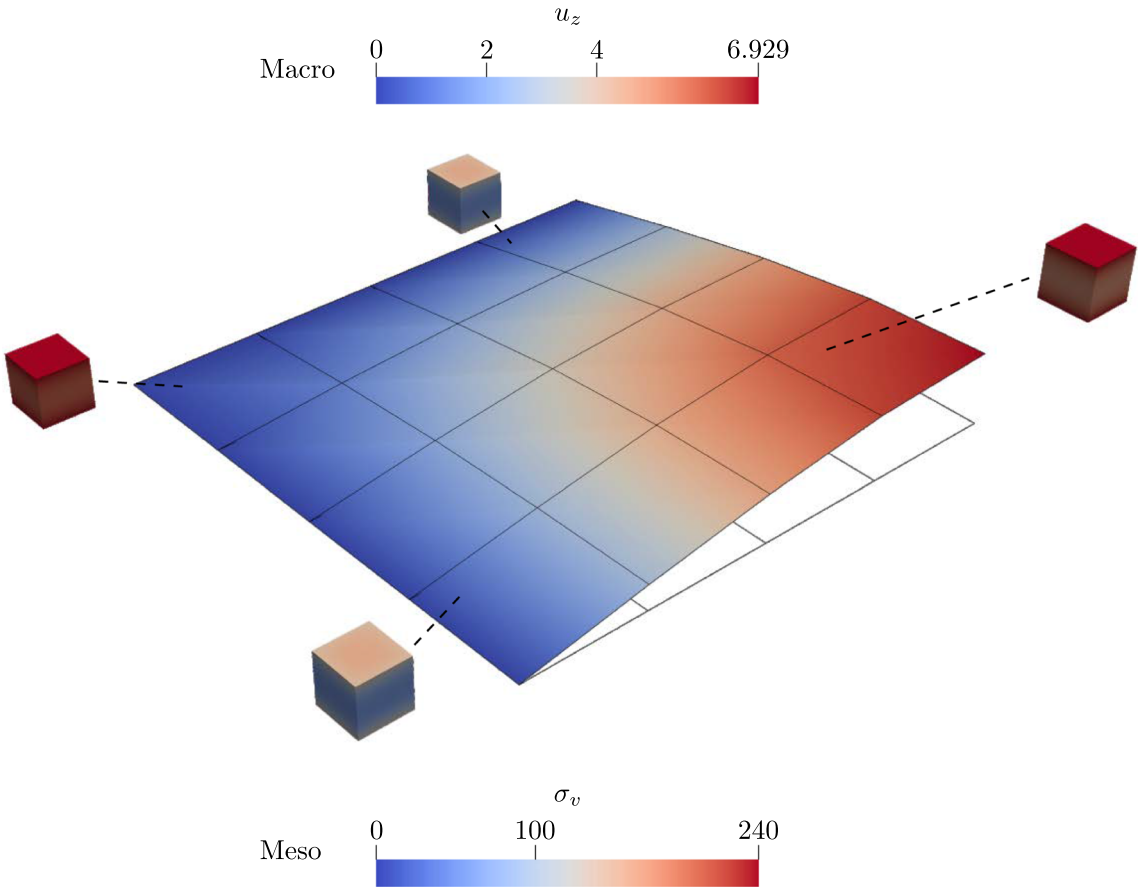

Fig. 29 Displacement u_z [cm] of the macroscopic shell and von Mises stress σ_v [kN/cm^2] of the RVEs ($\lambda = 14.4$)

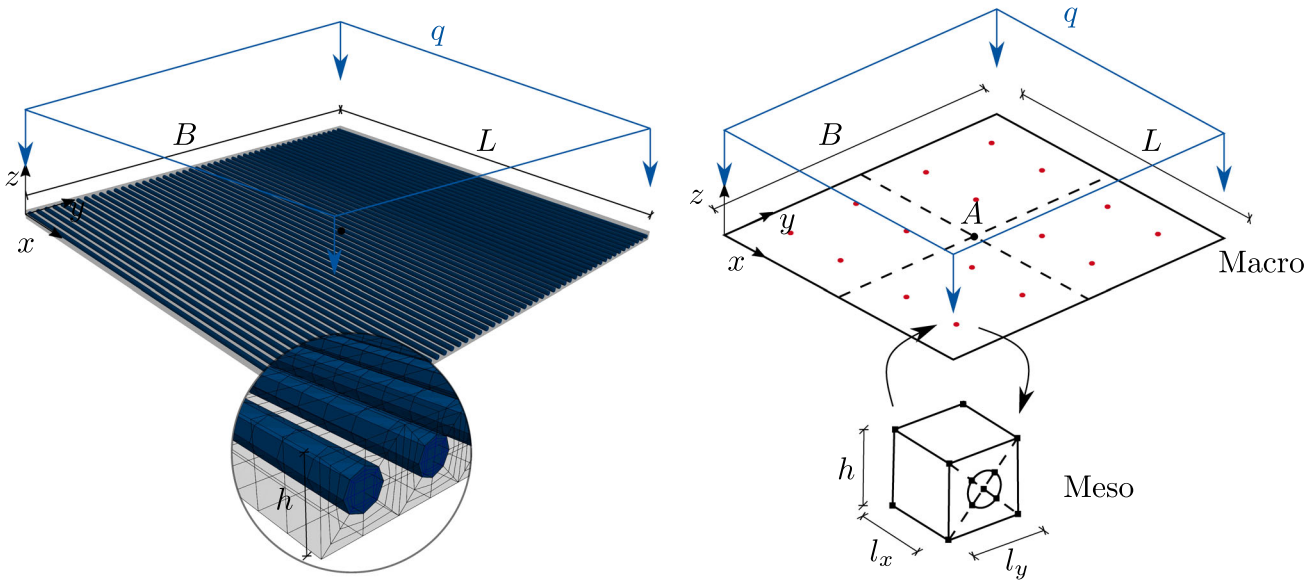

Fig. 30 Comparison of full-scale model (left) with homogenization approach (right) for plate [29]

Table 7 Boundary conditions for the plate

	Full-scale	Macroscale (FE^2)
$x = 0, y = 0$	$u_z = 0$	$u_z(z = 0) = 0$
$x = l/2$	$u_x = 0$	$u_x = 0, \omega_y = 0$
$y = b/2$	$u_y = 0$	$u_y = 0, \omega_x = 0$

significant length dependency. The traction boundary conditions, however, exhibit severe length dependency and seem to be unable to predict the correct behaviour. This is caused by the length dependency in torsional stiffness D_b^{33} which has already been observed in section 7.1.1, see Fig. 14a. Furthermore, Fig. 31 shows that the extensive macroscopic refinement is not necessary. For smaller numbers of macroscopic elements sufficiently accurate results can be obtained. To compare the efficiency of the homogenization approach to the full-scale model the complexity is used as measure for the computational effort. Taking into account the sparsity of the system of equations, e.g. by using the PARDISO solver, the number of equations can be reduced. The maximal num-

Table 8 Complexity of the different approaches

Full-scale model	FE^2
$\mathcal{O}(n_{eq}^2)$	$\mathcal{O}(n_{eq,M}^2 + n_{GP} \cdot n_{eq,m}^2)$

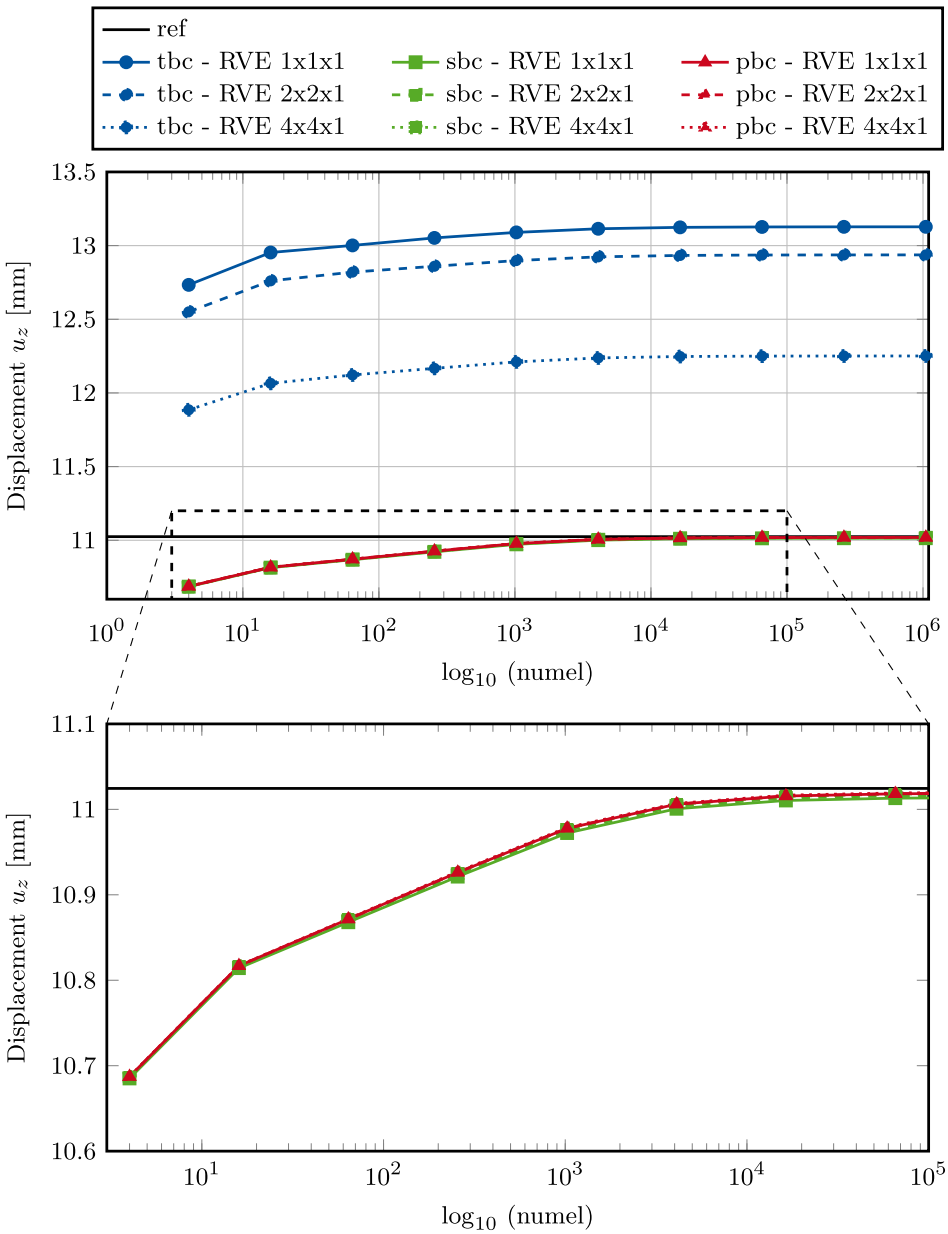

Fig. 31 Comparison of the vertical displacement in Point A for different macroscopic discretisations

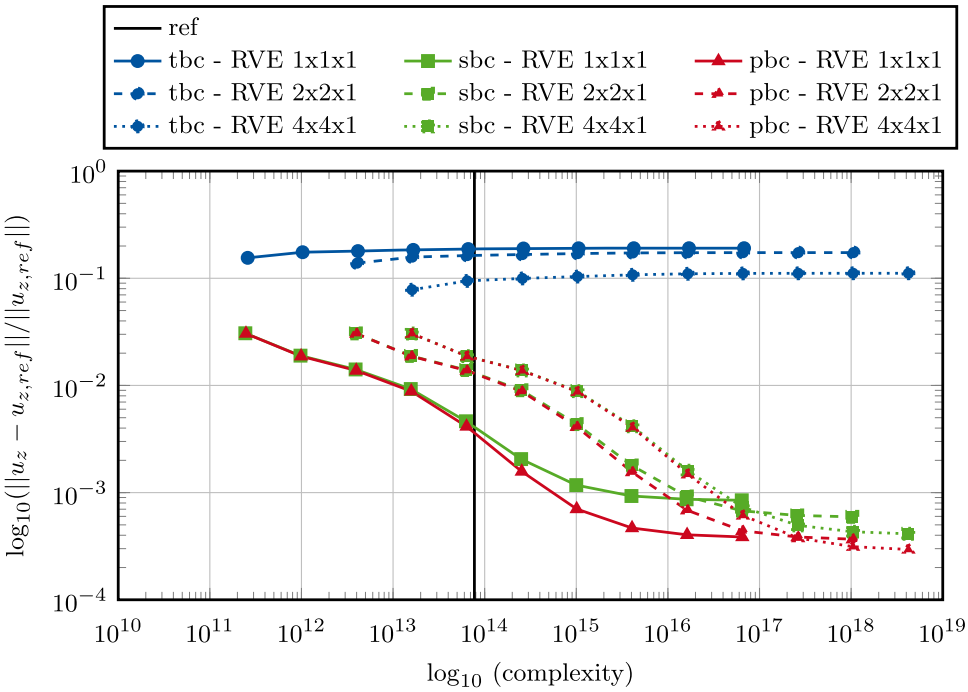

Fig. 32 Error of the FE^2 solution compared to the complexity for different RVE sizes

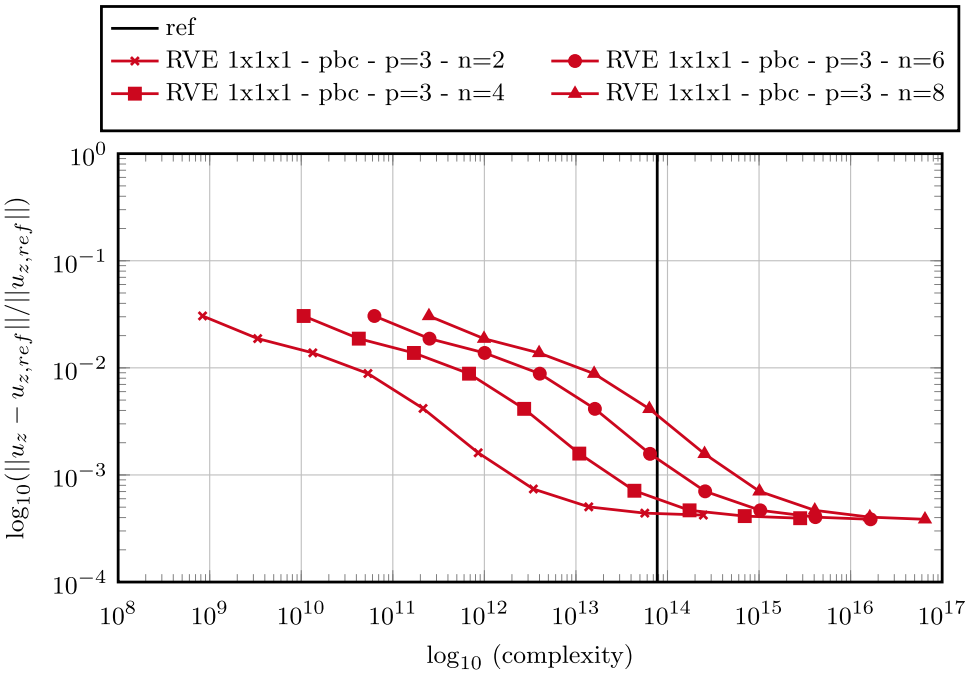

Fig. 33 Error of the FE^2 solution compared to the complexity for different discretisations of the RVE

ber of n^3 operations can be reduced to a complexity of about $\mathcal{O}(n^2)$ [19]. For the full-scale model the number of equations is the total number of equations in the system, while for the FE^2 approach it is the number of equations on the macroscopic scale plus the number of equations of the RVE times the number of Gauss points, see Table 8.

Figure 32 shows the error of the numerical solution to the full-scale solution and the corresponding complexity. The black, vertical line indicates the complexity of the full-scale model. A number of observations can be made. As has already become apparent from Fig. 31 the traction boundary conditions do not yield sufficient results and exhibit a strong length dependency. For the shell boundary conditions a small length dependency is observed. However, increasing the RVE size increases mainly the complexity of the problem without significant improvement in the results. The same observations can be made for periodic boundary conditions, where the differences in the quality of the solution are even smaller.

For the same complexity the coupled multiscale approach approximates the reference to about 0.4%, which is a good result keeping in mind, that full-scale solutions and shell computations hardly give the same results due to their different handling of boundary and loading conditions.

So far not much attention has been paid to the discretisation of the mesoscale. However, the more efficient the mesoscale is discretised the more efficient the solution of the coupled problem is carried out. To briefly emphasize the effect a RVE of size $1 \times 1 \times 1$ [cm×cm×cm] using periodic boundary conditions is discretised using polynomial order $p = 3$ and $n_c = n_b = 2, 4, 6, 8$ elements. Figure 33 shows, that the overall macroscopic behaviour is not significantly influenced. Whereas the complexity is approx. 300 times lower for the coarsest discretisation compared to the finest.

8 Conclusion

A first-order homogenization approach for shell structures has been presented. The macroscopic scale is discretised using quadrilateral shell elements while for the RVE scaled boundary isogeometric analysis was employed. However, the approach is not limited to this discretisation technique on the mesoscopic scale. It was chosen because isogeometric analysis promises a more accurate geometry description for complex mesostructures. A comparison regarding efficiency with other discretisation techniques was out of the scope of this work. Nevertheless, a more detailed investigation holds potential in further reducing the computational cost.

Three different sets of boundary conditions were introduced, which differ in the application of shell strains. These are either applied by prescribing displacements or by a prescribed rotation of the lateral surface by means of a transition element. Furthermore, a linear moment constraint is used to reduce the dependency of the transverse shear components on the RVE size. The assumption of linear moment distribution reaches its limits when the inhomogeneities of the mesostructure do not span the whole width of the RVE. It has been shown, that the incorporation of stiffness jumps over the height of the RVE is an important feature. The present work focuses on examples with homogeneous, layered or textile-reinforced RVEs. All heterogeneities are assumed to be uniformly distributed. Investigations on different mesoscopic geometries, e.g. with circular inclusions or randomly distributed heterogeneities, are still open. Furthermore, the additional constraints are formulated for small strains only, this could be extended in the future. The three boundary conditions were verified and differences with regard to their applicability were shown. On the mesoscale analytical stiffness components were reproduced with sufficient accuracy. Various macroscopic problems are presented and compared with full-scale solutions. Overall the periodic boundary conditions yield the best results, as the dependency of the transverse shear stiffness on the RVE size is reduced effectively and the results are in good agreement with reference solutions. However, the shell boundary conditions still yield sufficient results and small length dependency of the stiffness components, while being less complex compared to the periodic boundary conditions. This is due to the fact that no transition element is needed for the application of shear strains. The presented traction boundary conditions still show a large dependency of the torsional and shear stiffness components on the chosen RVE size, especially for bending-dominated problems. This increases the computational effort significantly. Nevertheless, the traction boundary conditions are valuable when investigating non-symmetric mesostructures.

Acknowledgements This work was funded by the Deutsche Forschungsgemeinschaft (DFG, German Research Foundation)-SFB/TRR 280. Project-ID: 417002380. The authors are grateful to the Center for Information Services and High Performance Computing [Zentrum für Informationsdienste und Hochleistungsrechnen (ZIH)] at TU Dresden for providing its facilities for high throughput calculations. We would like to thank Dr. Aewis Hii (Univeristy of Bristol) for sharing his research results.

Funding Open Access funding enabled and organized by Projekt DEAL.

Appendix A

An homogeneous representative volume element ($l_x = l_y = h = 1$ [mm]) with isotropic, linear elastic material behaviour ($E = 100$ [N/mm^2], $\nu = 0.3$) is considered. Each macroscopic shell strain, with a value of 0.2 in each case, is applied individually. For all three proposed boundary conditions the corresponding deformation figures are depicted in Figs. 34,35 and 36. The displacement magnitude is shown as contour plot, with blue and red indicating the minimum and maximum displacement, respectively. It can be seen, that the deformation modes for all membrane strains $\varepsilon_{\alpha,\beta}$ and curvatures $\kappa_{\alpha\beta}$, with $\alpha, \beta = x, y$, leads to reasonable deformation modes. Differences can only be observed regarding the deformation due to applied shear strains γ_α. The differences are treated in Sect. 6.4 in more detail.

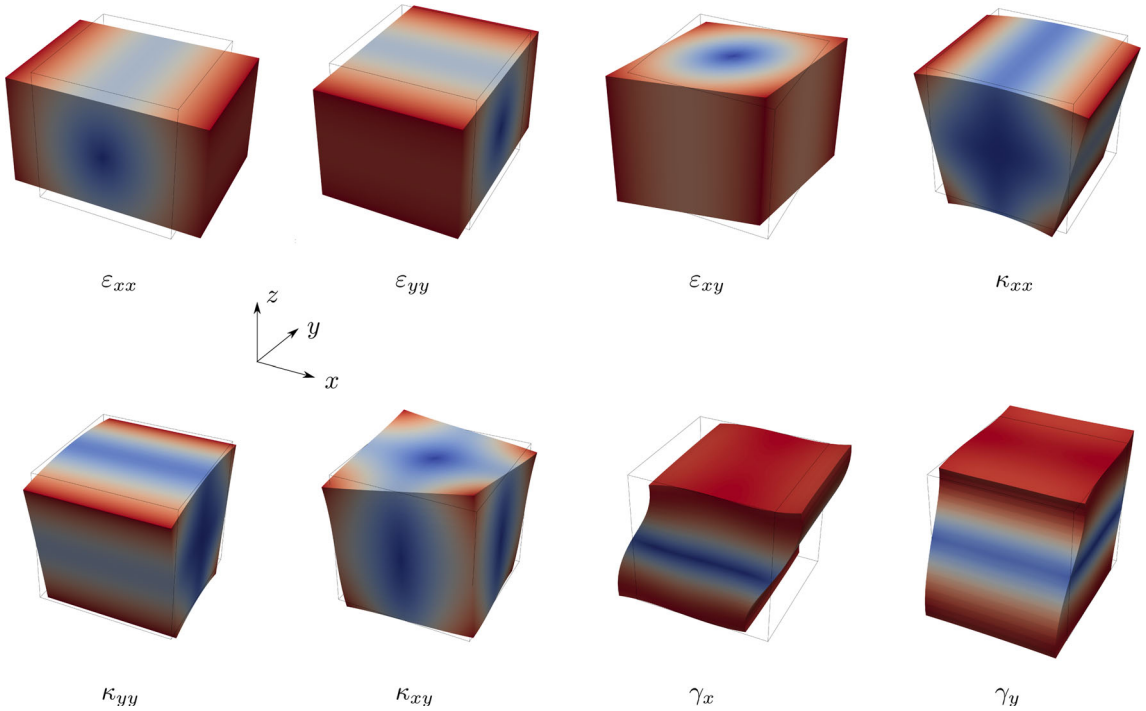

Fig. 34 Deformation modes of isotropic, homogeneous representative volume element with traction boundary conditions (tbc)

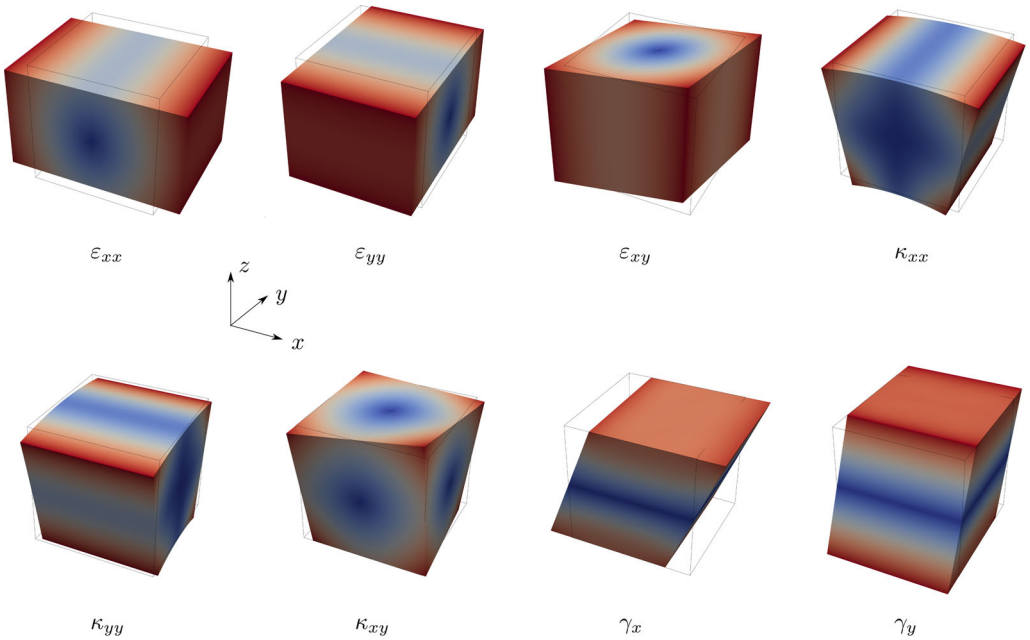

Fig. 35 Deformation modes of isotropic, homogeneous representative volume element with shell boundary conditions (sbc)

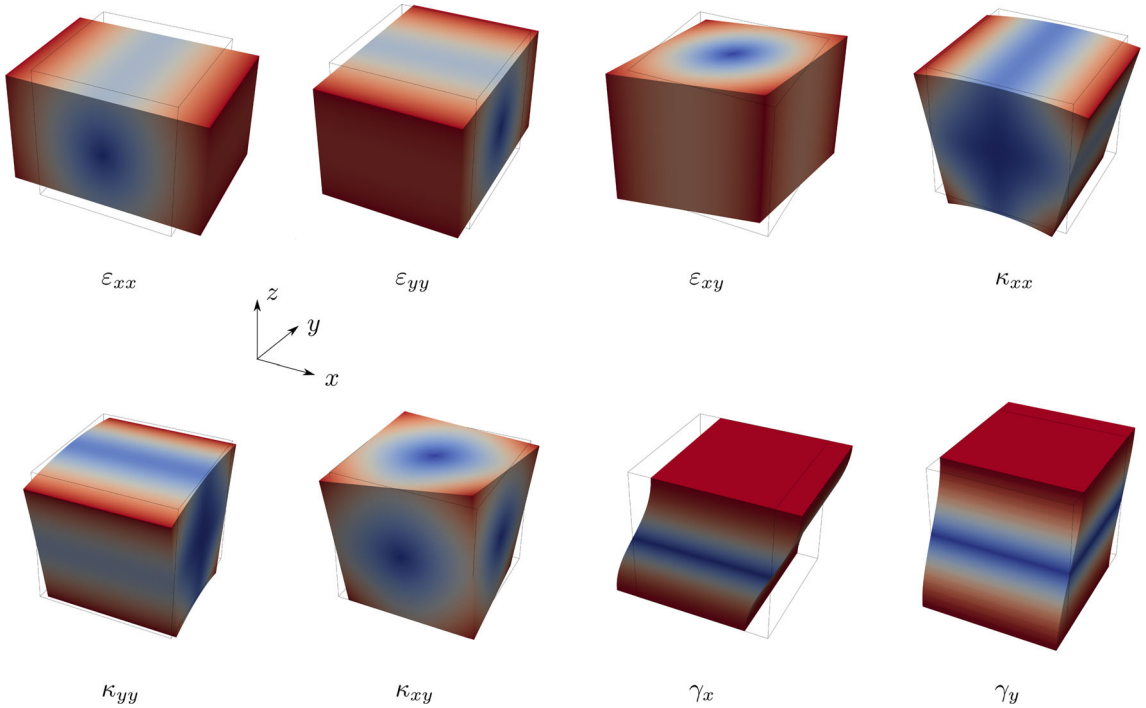

Fig. 36 Deformation modes of isotropic, homogeneous representative volume element with periodic boundary conditions (pbc)

Appendix B

To underline the necessity of the moment reduction constraint introduced in Sect. 5.4 which arises from the discussed inconsistency regarding the applied shear deformation, see Sect. 4.3, the introductory example from Sect. 7.1.1 is resumed. There, an homogeneous RVE with dimensions $1 \times 1 \times 1$ [mm×mm×mm] was considered. Again, linear elastic isotropic material with Young's Modulus $E = 100$ [N/mm^2] and Poisson's ratio $\nu = 0.3$ is assumed. Once more, the dimensions of $L^{RVE} = l_x = l_y$ are consecutively increased, while the height is kept constant, to investigate the influence of the length scale of the RVE. Figure 37 plots the resulting shear correction factor for different RVE sizes using periodic boundary conditions. The obtained shear stiffness tends to zero for increasing RVE sizes when no additional constraint is used. Employing the moment reduction constraint (abbreviated as MRC) leads to a constant shear correction factor of $\kappa = 5/6$ for increasing RVE sizes.

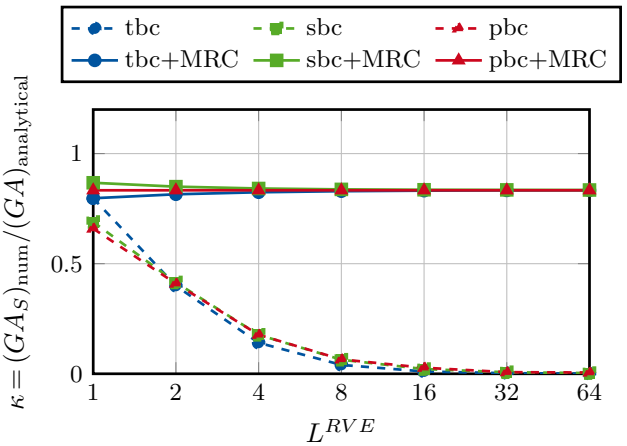

Fig. 37 Deformation modes of isotropic, homogeneous representative volume element with periodic boundary conditions (pbc)

References

1. Apostolatos A, Schmidt R, Wüchner R et al (2014) A nitsche-type formulation and comparison of the most common domain decomposition methods in isogeometric analysis. Int J Numer Meth Eng 97(7):473–504. https://doi.org/10.1002/nme.4568
2. Bauer B, Arioli C, Simeon B (2021) Generating star-shaped blocks for scaled boundary multipatch IGA. In: van Brummelen H, Vuik C, Möller M et al (eds) Isogeometric analysis and applications 2018, vol 133. Lecture notes in computational science and engineering. Springer, Cham, pp 1–25. https://doi.org/10.1007/978-3-030-49836-8_1
3. Börjesson E, Larsson F, Runesson K et al (2023) Variationally consistent homogenisation of plates. Comput Methods Appl Mech Eng 413(116):094. https://doi.org/10.1016/j.cma.2023.116094
4. Cartraud P, Messager T (2006) Computational homogenization of periodic beam-like structures. Int J Solids Struct 43(3–4):686–696. https://doi.org/10.1016/j.ijsolstr.2005.03.063
5. Chasapi M, Klinkel S (2018) A scaled boundary isogeometric formulation for the elasto-plastic analysis of solids in boundary representation. Comput Methods Appl Mech Eng 333:475–496. https://doi.org/10.1016/j.cma.2018.01.015
6. Chasapi M, Klinkel S (2020) Geometrically nonlinear analysis of solids using an isogeometric formulation in boundary representation. Comput Mech 65(2):355–373. https://doi.org/10.1007/s00466-019-01772-6
7. Chasapi M, Dornisch W, Klinkel S (2020) Patch coupling in isogeometric analysis of solids in boundary representation using a mortar approach. Int J Numer Meth Engng 121(14):3206–3226. https://doi.org/10.1002/nme.6354
8. Chasapi M, Mester L, Simeon B et al (2021) Isogeometric analysis of 3D solids in boundary representation for problems in nonlinear solid mechanics and structural dynamics. Int J Numer Meth Engng. https://doi.org/10.1002/nme.6893
9. Chen L, Dornisch W, Klinkel S (2015) Hybrid collocation-Galerkin approach for the analysis of surface represented 3D-solids employing SB-FEM. Comput Methods Appl Mech Eng 295:268–289. https://doi.org/10.1016/j.cma.2015.07.004
10. Chen L, Simeon B, Klinkel S (2016) A NURBS based Galerkin approach for the analysis of solids in boundary representation. Comput Methods Appl Mech Eng 305:777–805. https://doi.org/10.1016/j.cma.2016.03.019
11. Coenen E, Kouznetsova V, Geers M (2010) Computational homogenization for heterogeneous thin sheets. Int J Numer Meth Eng 83(8–9):1180–1205. https://doi.org/10.1002/nme.2833
12. Cong Y, Nezamabadi S, Zahrouni H et al (2015) Multiscale computational homogenization of heterogeneous shells at small strains with extensions to finite displacements and buckling. Int J Numer Meth Eng 104(4):235–259. https://doi.org/10.1002/nme.4927
13. Cottrell JA, Hughes TJR, Bazilevs Y (2009) Isogeometric analysis: toward integration of CAD and FEA. Wiley, Hoboken
14. Dornisch W, Vitucci G, Klinkel S (2015) The weak substitution method - an application of the mortar method for patch coupling in NURBS-based isogeometric analysis. Int J Numer Meth Eng 103(3):205–234. https://doi.org/10.1002/nme.4918
15. Dvorkin E, Bathe KJ (1984) A continuum mechanics based four-node shell element for general non-linear analysis. Eng Comput 1(1):77–88. https://doi.org/10.1108/eb023562
16. Feyel F, Chaboche JL (2000) FE2 multiscale approach for modelling the elastoviscoplastic behaviour of long fibre SiC/Ti composite materials. Comput Methods Appl Mech Eng 183(3–4):309–330. https://doi.org/10.1016/S0045-7825(99)00224-8
17. Geers M, Coenen E, Kouznetsova V (2007) Multi-scale computational homogenization of structured thin sheets. Model Simul Mater Sci Eng 15(4):S393–S404. https://doi.org/10.1088/0965-0393/15/4/S06
18. Geers M, Kouznetsova V, Brekelmans W (2010) Multi-scale computational homogenization: trends and challenges. J Comput Appl Math 234(7):2175–2182. https://doi.org/10.1016/j.cam.2009.08.077
19. Golub GH, van Loan CF (2013) Matrix computations, 4th edn. Johns Hopkins studies in the mathematical sciences. The Johns Hopkins University Press, Baltimore
20. Gruttmann F, Wagner W (2006) Structural analysis of composite laminates using a mixed hybrid shell element. Comput Mech 37(6):479–497. https://doi.org/10.1007/s00466-005-0730-1
21. Gruttmann F, Wagner W (2013) A coupled two-scale shell model with applications to layered structures. Int J Numer Meth Eng 94(13):1233–1254. https://doi.org/10.1002/nme.4496
22. Heller D (2016) A nonlinear multiscale finite element model for comb-like sandwich panels. Dissertation, Technische Universität Darmstadt. https://tuprints.ulb.tu-darmstadt.de/id/eprint/5288
23. Hii AK, El Said B (2022) A kinematically consistent second-order computational homogenisation framework for thick shell models. Comput Methods Appl Mech Eng 398:115–136. https://doi.org/10.1016/j.cma.2022.115136
24. Hill R (1963) Elastic properties of reinforced solids: some theoretical principles. J Mech Phys Solids 11(5):357–372. https://doi.org/10.1016/0022-5096(63)90036-X
25. Hughes TJR, Cottrell JA, Bazilevs Y (2005) Isogeometric analysis: CAD, finite elements, NURBS, exact geometry and mesh refinement. Comput Methods Appl Mech Eng 194(39–41):4135–4195. https://doi.org/10.1016/j.cma.2004.10.008
26. Hughes TJR, Reali A, Sangalli G (2010) Efficient quadrature for NURBS-based isogeometric analysis. Comput Methods Appl Mech Eng 199(5–8):301–313. https://doi.org/10.1016/j.cma.2008.12.004
27. Klarmann S (2018) Geometrisch und physikalisch nichtlineare Mehrskalenmodellierung räumlicher Stabtragwerke. Dissertation, Technische Universität Darmstadt, https://tuprints.ulb.tu-darmstadt.de/id/eprint/7638
28. Klarmann S, Gruttmann F, Klinkel S (2020) Homogenization assumptions for coupled multiscale analysis of structural elements: Beam kinematics. Comput Mech 65:635–661. https://doi.org/10.1007/s00466-019-01787-z
29. Mester L, Wagner F, Liebold F, et al (2022) Image-based modelling and analysis of carbon-fibre reinforced concrete shell structures. In: Stokkeland S (ed) Concrete innovation for sustainability. In: Proceedings, International Federation for Structural Concrete, Lausanne, Switzerland, pp 1631–1640
30. Mester L, Klarmann S, Klinkel S (2023) Homogenisation for macroscopic shell structures with application to textile-reinforced mesostructures. Proc Appl Math Mech. https://doi.org/10.1002/pamm.202200137
31. Müller M, Klarmann S, Gruttmann F (2022) A new homogenization scheme for beam and plate structures without a priori requirements on boundary conditions. Comput Mech 70:1167–1187. https://doi.org/10.1007/s00466-022-02219-1
32. Natarajan S, Wang J, Song C et al (2015) Isogeometric analysis enhanced by the scaled boundary finite element method. Comput Methods Appl Mech Eng 283:733–762. https://doi.org/10.1016/j.cma.2014.09.003
33. Piegl L, Tiller W (1997) The NURBS Book. Springer, Berlin. https://doi.org/10.1007/978-3-642-59223-2
34. Praster M, Klassen M, Klinkel S (2019) An adaptive FE^2 approach for fiber-matrix composites. Comput Mech 63(6):1333–1350. https://doi.org/10.1007/s00466-018-1652-z
35. Saeb S, Steinmann P, Javili A (2016) Aspects of computational homogenization at finite deformations: a unifying review from

Reuss' to Voigt's bound. Appl Mech Rev 68:5. https://doi.org/10.1115/1.4034024
36. Song C, Wolf JP (1997) The scaled boundary finite-element method–alias consistent infinitesimal finite-element cell method–for elastodynamics. Comput Methods Appl Mech Eng 147(3–4):329–355. https://doi.org/10.1016/S0045-7825(97)00021-2
37. Taylor R (2003) FEAP—a finite element analysis program. https://www.projects.ce.berkeley.edu/feap/
38. Terada K, Hirayama N, Yamamoto K et al (2016) Numerical plate testing for linear two-scale analyses of composite plates with in-plane periodicity. Int J Numer Meth Eng 105(2):111–137. https://doi.org/10.1002/nme.4970
39. Vlachoutsis S (1992) Shear correction factors for plates and shells. Int J Numer Meth Eng 33(7):1537–1552. https://doi.org/10.1002/nme.1620330712
40. Wagner W, Gruttmann F (2005) A robust non-linear mixed hybrid quadrilateral shell element. Int J Numer Meth Eng 64(5):635–666. https://doi.org/10.1002/nme.1387
41. Wüst J, Wagner W (2008) Systematic prediction of yield-line configurations for arbitrary polygonal plates. Eng Struct 30(7):2081–2093. https://doi.org/10.1016/j.engstruct.2008.01.005